Polymer Chemistry

ROYAL SOCIETY OF CHEMISTRY

PAPER

View Article Online
View Journal | View Issue

Cite this: *Polym. Chem.*, 2026, **17**, 216

Graphene oxide-*graft*-poly(2-(dimethylamino) ethyl methacrylate) as a functional additive for structurally tuned and high-performance thin-film composite membranes

Reza Razavi,[a] Alireza Shakeri, *[a] Hasan Salehi,[a] Rozgol Bonsale,[b] Amir Jangizehi[c] and Sebastian Seiffert *[c]

Forward osmosis (FO), a pressure-free membrane process, holds significant promise for water purification and seawater desalination. However, its efficiency is often limited by internal concentration polarization (ICP). To address this challenge, high-performance thin-film nanocomposite (TFN) membranes were developed by modifying poly(ethersulfone) (PES) substrates with varying amounts of graphene oxide-*graft*-poly(2-dimethylaminoethyl methacrylate) (GO-*g*-PDMA) nanoplates. The PDMA polymer is synthesized *via* atom transfer radical polymerization (ATRP) and covalently grafted onto azide-functionalized GO *via* click chemistry. This study systematically investigates the effects of GO-*g*-PDMA loading on substrate morphology, polyamide (PA) active layer formation, and overall membrane performance. Compared to bare GO, GO-*g*-PDMA significantly enhances the PES substrate's hydrophilicity, porosity, and water permeability. The optimally loaded TFN membrane (0.5 wt% GO-*g*-PDMA) exhibits superior FO performance, achieving water fluxes of 27.8 ± 1.9 L m^{-2} h^{-1} (LMH) in FO mode and 52.1 ± 1.5 LMH in PRO mode. Importantly, this membrane also demonstrates a 53.4% reduction in the structural parameter (*S*) relative to the unmodified TFC membrane, underscoring its improved resistance to ICP. These findings highlight the potential of GO-*g*-PDMA-functionalized substrates for enhancing FO membrane performance through synergistic improvements in the structure and function.

Received 18th June 2025,
Accepted 3rd November 2025

DOI: 10.1039/d5py00605h

rsc.li/polymers

1. Introduction

Providing sufficient potable water is essential for the sustainability of industrial operations and human life. In light of rapid population growth and the limited availability of global freshwater resources, cost-efficient and rapid seawater desalination and wastewater treatment have become increasingly important to meet the demand for high-quality water across sectors.[1] The development of advanced processes with low operating costs and minimal energy consumption holds promise for enabling sustainable potable water production from unconventional sources.[2] Forward osmosis (FO) has recently attracted considerable attention as a novel membrane-based technology in both industrial applications and academic research.[3] The FO process involves two solutions with differing osmotic pressures: the draw solution (DS), which possesses a higher osmotic pressure, and the feed solution (FS), which has a lower osmotic pressure.[4] During FO, the osmotic pressure gradient drives water to permeate through the FO membrane toward the DS side while limiting solute passage.[5] The FO process is widely favored for its low energy consumption, high water recovery potential, and relatively low fouling propensity.[6,7] These advantages make FO technology highly attractive and widely applied across diverse fields, including food processing, seawater desalination, power generation, pharmaceutical intermediate enrichment, and wastewater treatment.. Although FO offers several advantages over pressure-driven membrane technologies, it still encounters major limitations, including: (1) intrinsic membrane shortcomings, (2) difficulties in recovering water from diluted draw solutions, and (3) concentration polarization (CP) effects that obstruct industrial-scale application.[8] Advancing high-performance membranes is considered a crucial step toward the successful commercialization of FO technology. Numerous studies have aimed to develop FO membranes that deliver high water permeability along with minimal reverse salt flux.[9–11] Commonly, FO membranes are prepared using different approaches, such as (i) the layer-by-layer (LBL) self-assembly technique,[12] (ii) thin-film composite (TFC)

[a]*School of Chemistry, College of Science, University of Tehran, 14155-6619 Tehran, Iran. E-mail: Alireza.shakeri@ut.ac.ir*
[b]*Environmental and Chemical Engineering Unit, Faculty of Technology, University of Oulu, Oulu, Finland*
[c]*Department of Chemistry, Johannes Gutenberg University of Mainz, Duesbergweg 10-14, 55128 Mainz, Germany. E-mail: Sebastian.seiffert@uni-mainz.de*

membranes fabricated through interfacial polymerization (IP), and (iii) self-standing PA rejection layers formed without a supporting substrate.[13] Among these, TFC-FO membranes are widely used for their superior solute rejection, high water permeability, and resistance over a broad pH range.[14] The fabrication of TFC-FO membranes typically involves two main steps: (1) creation of a porous substrate *via* non-solvent induced phase separation (NIPS), and (2) IP reaction between m-phenylenediamine (MPD) in the aqueous phase and trimesoyl chloride (TMC) in hexane to form the PA selective layer.[15] Each layer in the TFC-FO membrane architecture plays a distinct and essential role in boosting the overall separation performance. The substrate mainly governs the structural stability of the TFC membrane during FO, while the PA active layer determines the membrane's selectivity. In the FO mode with the active layer facing the feed solution (ALFS orientation), water permeation dilutes the draw solution at the PA–support interface, significantly lowering the effective osmotic pressure gradient and thus reducing water flux due to internal concentration polarization (ICP).[16] ICP is strongly affected by substrate characteristics such as tortuosity, porosity, and thickness. These factors are collectively described by the structural parameter (S).[15] A lower S value indicates reduced ICP effects and improved FO membrane performance. Recently, extensive research has focused on minimizing ICP by developing TFC-FO membranes with highly porous, thin substrates and improving substrate hydrophilicity through techniques such as surface modification,[17] template-assisted fabrication,[18] blending with hydrophilic additives,[19] and nanomaterial incorporation.[20] In recent years, integrating hydrophobic polymer substrates with hydrophilic nanomaterials to tailor substrate properties has emerged as a promising strategy for enhancing FO membranes. Various inorganic and organic nanostructures have been utilized for this purpose, including layered-double hydroxides,[21] ZnO-SiO_2 core–shell nanoparticles,[22] graphene oxide (GO),[23] MoS_2,[24] quaternary GO,[25] carbon nanotubes,[26] metal–organic frameworks,[27] and amine-functionalized zinc oxide.[28] Among them, GO nanosheets have gained attention as effective membrane materials owing to their oxygen-rich surface functionalities (carboxyl, epoxy, and hydroxyl groups), which impart excellent hydrophilicity and tunable surface chemistry. Although GO-incorporated nanocomposite substrates exhibit excellent permeability and hydrophilicity, the limited affinity between hydrophobic substrates and hydrophilic GO nanoplates must be carefully addressed.[29] This weak compatibility between the polymer substrate and GO nanoplates can negatively impact the mechanical strength and stability of the nanocomposite support layers during the FO process. Additionally, achieving uniform dispersion of GO nanoplates remains a significant challenge due to their high surface energy, which results from competing entropic (π–π stacking) and enthalpic (hydrogen bonding) interactions[29]. Surface functionalization of GO is considered an effective strategy to overcome this issue. For instance, the "polymer grafting to" technique is recognized as a suitable method to reduce GO aggregation within the polymer matrix.[30] To date, various GO-based nanofillers have been modified with different polymers and applied to membrane modification, including GO-*g*-PHEMA,[31] GO-*g*-PSBMA,[32] GO-CS,[33] and PEG-*g*-GO.[34] Among these functional modifiers, hydrophilic polymers such as poly(2-(dimethylamino)ethyl acrylate) (PDMA) have gained attention as promising candidates due to their excellent functionalization capacity and interfacial compatibility.[30]

Based on this background, in this investigation, we developed a novel TFN-FO membrane utilizing PDMA-*graft*-GO (GO-*g*-PDMA) nanoplates as blending nanofillers. The GO-*g*-PDMA nanofillers were successfully prepared *via* a click reaction by grafting alkynyl-PDMA brushes onto GO-N_3 nanoplates, and the resulting nanofillers were thoroughly analyzed. Five nanocomposite substrates were then constructed by incorporating GO and GO-*g*-PDMA in varying amounts *via* the NIPS method. Subsequently, the PA rejection layer was established on the nanocomposite substrates to obtain the TFN-FO membranes. We examine in detail the effects of GO or GO-*g*-PDMA nanofillers on the substrate and PA active-layer properties, including further assessment of how variations in the substrate and PA rejection layer influence the FO efficiency of the TFN-FO membranes.

Sebastian Seiffert

Sebastian Seiffert is a full professor for physical chemistry of polymers at Johannes Gutenberg-University Mainz. He is spokesperson of a DFG Research Unit on amphiphilic co-networks, of a BMBF Project on seawater desalination by hydrogels, and of a DFG Collaborative Research Center on defects in soft matter. He is also the author of several textbooks on physical chemistry and polymer science. Sebastian's work was honored with the Reimund Stadler Award of the German Chemical Society, an annual award by the Association of German University Professors in Chemistry, a young investigator award by the Polymer Networks Group, and the Ars-legendi Faculty Award for excellence in teaching.

2. Experimental

2.1. Materials

Graphite powder, supplied by Alfa Aesar Company, was used for the synthesis of GO nanoplates. Potassium permanganate ($KMnO_4$, 99%), sulfuric acid (H_2SO_4, 98%), hydrogen peroxide (H_2O_2, 30%), phosphoric acid (H_3PO_4, 99%), and hydrochloric acid (HCl, 37%) were procured from Merck and employed in the preparation of GO nanoplates. Sodium azide (NaN_3, Merck), (3-glycidyloxypropyl) trimethoxysilane (GPTMS, Merck), and ethanol (C_2H_5OH, ≥99.9%, Merck) were used to synthesize azide-functionalized GO (GO-N_3) nanoplates. For the synthesis of alkyne-terminated PDMA polymer, propargyl

2-bromoisobutyrate (PBiB, 98%) was used as the initiator, (2-dimethylamino)ethyl methacrylate (DMA, 98%) as the monomer, copper(I) bromide (CuBr, 99%) as the catalyst, *N*,*N*,*N*′,*N*′,*N*″-pentamethyl diethylene triamine (PMDETA, 98%) as the ligand, and dimethyl formamide (DMF, 98%) as the solvent—all obtained from Merck. Polyethersulfone (PES) powder (M_w = 58 000 g mol^{-1}, Ultrason® E 6020, BASF Co., Germany) was used as the polymeric support, while polyethylene glycol (PEG, M_w = 400 g mol^{-1}, Merck, Germany) serves as the pore-forming agent. *N*-Methyl-2-pyrrolidone (NMP, Merck) is used as the solvent for fabricating the support layers. Two monomers, water-soluble m-phenylenediamine (MPD) and hexane-soluble trimesoyl chloride (TMC), were provided by Merck and used to form the PA layer on the support through the IP process. Anhydrous *n*-hexane (≥99.9%, Merck) and deionized (DI) water were used to prepare the aqueous MPD and organic TMC solutions. Sodium chloride (NaCl, 99%) was purchased from Merck and used to prepare draw solutions (DS) at various concentrations for FO performance evaluation.

2.2. GO synthesis

GO nanoplates were synthesized using a modified Hummers' method.[35] In this method, an acidic mixture (9 : 1) of 20 mL of H_3PO_4 and 180 mL of H_2SO_4 was first prepared. Then, 1.5 g of graphite powder and 9.0 g of $KMnO_4$ were added to the acidic solution, and the mixture was stirred at 35–40 °C. The acidic suspension was then stirred at 50 °C for 24 h. After this period, the mixture was allowed to cool to room temperature. Subsequently, 200 mL of cold DI water containing 1.5 mL of H_2O_2 was added. Under continuous stirring, an orange-yellow suspension formed. This suspension was centrifuged at 4000 rpm for 4 h, and the supernatant was decanted. The acidic GO gel was then stirred in 30% HCl solution for 8 h, rinsed multiple times with ethanol and DI water, and recovered *via* centrifugation. Finally, the purified GO gel was dried in a freeze dryer for 24 h.

2.3. Azide-functionalization of GO nanoplates (GO-N_3)

GO-N_3 nanoplates were synthesized in two steps: (i) covalent grafting of GPTMS onto GO nanoplates *via* the reaction with –OH groups, and (ii) a ring-opening reaction between sodium azide and the epoxy ring. In a 200 mL dried round-bottomed flask, 1.0 g of as-prepared GO nanoplates was dispersed in 100 mL of anhydrous ethanol and stirred for 1 h to form a uniform suspension. Next, 0.1 g of GPTMS was added to the brownish GO suspension, and a silane-functionalization reaction was carried out at 70 °C for 12 h. To produce GO-N_3 nanoplates, 0.6 g of NaN_3 was introduced into the reaction mixture, and stirring was continued at 70 °C. After 12 h, the reaction was terminated. The resulting GO-N_3 nanoplates were collected using three repeated cycles of centrifugation (4000 rpm, 10 min) and redispersion (15 min) in DI water and ethanol, followed by drying in a vacuum oven at 40 °C.

2.4. Synthesis of alkynyl-terminated PDMA

In this work, an alkyne-terminated PDMA homopolymer was synthesized *via* ATRP using alkyne-terminated PBiB as the initiator (Fig. 1a). Specifically, 103 mg (0.5 mmol) of PBiB, 7.86 g (50 mmol) of DMA, 35.8 mg (0.25 mmol) of CuBr, and 104 μL (0.5 mmol) of PMDETA were combined in a 50 mL Schlenk flask containing 20 mL of dry DMF. The reaction system was degassed three times using a freeze–pump–thaw cycle, followed by ATRP polymerization at 80 °C for 12 h. The polymerization was terminated by adding 100 mL of water, and the reaction mixture was heated to 80 °C to induce precipitation of the PDMA polymer. For further purification, the PDMA polymer was dissolved in THF and passed through an alumina column to remove any residual Cu^+. The purified polymer solution was then concentrated by rotary evaporation and precipitated with hexane as the nonsolvent. ^{1}HNMR ($CDCl_3$): 1.0 ppm (9H, $-CH_3$), 1.8 ppm (2H, $-CH_2-$), 2.4 ppm (6H, $-N(CH_3)_2$), and 2.6 ppm (2H, $-N-CH_3-$).[36]

2.5. Preparation of GO-*g*-PDMA nanoplates

In this study, alkynyl-PDMA chains were grafted onto GO-N_3 nanoplates at a 1 : 1 mass ratio of GO to PDMA *via* a click reaction. To initiate the process, 0.6 g of GO-N_3 was dispersed in 20 mL of DMF containing 0.6 g (0.23 mmol) of alkyne-terminated PDMA, 0.025 g (0.18 mmol) of CuBr, and 0.04 g (0.23 mmol) of PMDETA, while nitrogen was bubbled through the mixture. The reaction proceeded at 25 °C for 72 h. Following the grafting step, the resulting PDMA-functionalized GO nanoplates were isolated by centrifugation (5000 rpm for 10 min), thoroughly rinsed with DMF and DI water, and subsequently dried in a vacuum oven at 50 °C. The final product was labeled as GO-*g*-PDMA.

2.6. Preparation of the nanocomposite substrates

In this work, all substrates, both pristine and nanocomposite, were fabricated using the conventional NIPS method. PES was employed as the polymer support, anhydrous NMP as the solvent, PEG-400 as the pore-forming agent, and GO or GO-*g*-PDMA as the nanofillers. DI water was used as the non-solvent coagulation bath. Prior to solution preparation, PES powder was dried at 70 °C for 12 hours to eliminate any surface-adsorbed moisture. A predetermined amount of nanoplates (either GO or GO-*g*-PDMA) was dispersed into a premixed solution of NMP and PEG, followed by 2 hours of sonication to ensure a stable, uniform suspension. Subsequently, PES powder was added to the casting solution and dissolved at 80 °C under continuous stirring. After complete dissolution, the solution was left undisturbed overnight to allow any trapped air bubbles to escape. The degassed casting solution was then cast onto a clean glass plate using a doctor blade with a 100 μm gap, and the plate was immediately immersed in a DI-water bath for 1 hour. Once solidified, the flat sheet substrates were transferred to a fresh DI-water coagulation bath and soaked for 24 hours to guarantee thorough solvent exchange between NMP and DI-water. Finally, the resulting substrates were stored in DI-water until further use in the IP reaction and characterization steps.

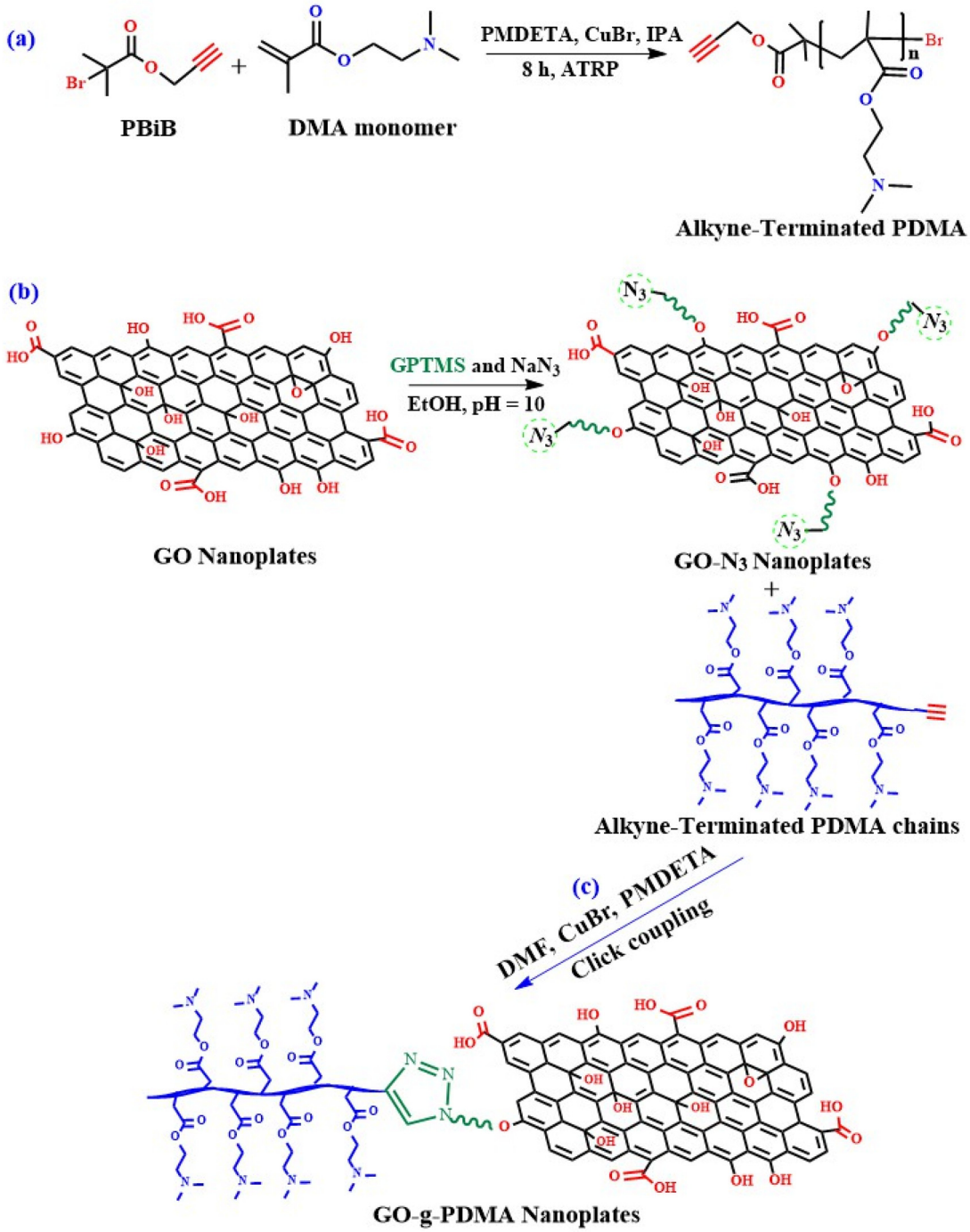

Fig. 1 Schematic representation of the synthetic route for GO-*g*-PDMA nanoplates.

2.7. Fabrication of a PA rejection layer

TFC and TFN-FO membranes were prepared *via* the IP reaction between TMC in the organic phase and MPD in the aqueous phase on pure and nanocomposite PES substrates, respectively. Initially, optimal concentrations of MPD (2.0 wt%) and TMC (0.1 wt%) were dissolved in DI water and *n*-hexane, respectively. The top surface of the nanocomposite PES substrate was taped onto a clean glass plate and soaked in the MPD solution for 2 minutes. After removing residual MPD droplets from the substrate surface using an air knife, the MPD-absorbed substrate was immersed in the TMC solution for 90 seconds to form the PA thin film. To remove unreacted TMC monomer, the formed PA skin layer was gently rinsed with *n*-hexane. The fabricated TFN membrane was then placed in an oven at 60 °C for 1 minute to ensure the formation of a stable, cross-linked PA active layer. After

washing the PA surface with DI water, all as-fabricated TFC and TFN membranes were stored in a DI water bath at 4 °C before structural characterization and performance testing. The unmodified TFC-FO membrane was fabricated following the same procedure without the addition of nanoplates. A TFC-FO membrane made from the pure PES substrate was used as the control.

2.8. Characterization of the prepared GO and GO-*g*-PDMA nanoplates

The GO, GO-N_3, and GO-*g*-PDMA nanoplates were analyzed using Fourier transform infrared spectroscopy (FTIR, Bruker, Equinox 55) to investigate their chemical compositions in the 400–3900 cm^{-1} range. X-ray diffraction (XRD) analysis was used to characterize the crystalline structure of the GO-*g*-PDMA nanoplates by using a PHILIPS PW1730 diffractometer from the Netherlands, with Cu Kα radiation (λ = 1.54056 Å) at 40 kV and 30 mA. Data collection covered a 2θ range of 7° to 60°, using a step size of 0.05° and a counting time of 1 second per step. Field-emission scanning electron microscopy (FE-SEM; Tescan VEGA) was used to observe morphological differences between GO and GO-*g*-PDMA nanoplates. Prior to SEM analysis, GO and GO-*g*-PDMA samples were dispersed in ultrapure ethanol by sonication and then deposited onto aluminum foil. The dried samples were gold-sputtered to enhance conductivity. Elemental analysis of GO-*g*-PDMA nanosheets was performed using energy dispersive spectroscopy (EDS) coupled with SEM. Thermal properties of the nanoplates (GO, GO-N_3, and GO-*g*-PDMA) were investigated by thermogravimetric analysis (TGA, Q600, TA, USA) under an inert atmosphere. Approximately 5 mg of each sample was heated from room temperature to 600 °C at 10 °C min^{-1}, and the polymer graft content was calculated from the mass loss.

2.9. Membrane characterization

The chemical compositions of the substrates and their corresponding PA active layers were characterized using attenuated total reflectance Fourier transform infrared spectroscopy (ATR-FTIR, Bruker, Equinox). Spectra are recorded over the wavenumber range of 600–2300 cm^{-1}. The morphology of the substrates' top and bottom surfaces, and their cross-sections, as well as the top surface of the PA layer, was examined using scanning electron microscopy (SEM, Tescan, VEGA). For cross-sectional imaging, samples were immersed in ethanol, fractured in liquid nitrogen, and then coated with a thin platinum layer to enhance conductivity. Energy-dispersive spectroscopy (EDS) analysis was performed to investigate the distribution of GO-*g*-PDMA nanosheets within the substrate structure, and elemental-mapping images were generated to visualize their dispersion throughout the TFN-FO membrane.

The surface roughness of the substrates and PA thin layers was measured in tapping mode using atomic force microscopy (AFM, Solver, NT-MDT). Membrane samples (~2 cm^2) were fixed to the sample holder and scanned over a 5 μm × 5 μm area. Membrane hydrophilicity was evaluated by water contact angle (WCA) measurements using the sessile drop method with a goniometer (CAG-20 SE, JIKAN, Iran). Membranes were dried in an oven until reaching a stable weight before testing. A 2 μL droplet of ultrapure water was placed on the membrane surface, and images were captured with a digital camera. Each membrane was analyzed at three random locations to minimize experimental error.

Substrate porosity (ε, %) was determined using the gravimetric method. Substrates were removed from DI water, surface water was gently blotted, and they were immediately weighed. Samples were then dried at 50 °C until constant weight was achieved. Porosity was calculated using eqn (1):

$$\varepsilon = \frac{(m_w - m_d)/\rho_W}{(m_w - m_d)/\rho_W + m_d/\rho_P} \quad (1)$$

where m_w and m_d are the weights of wet and dry substrates, respectively; ρ_W is the density of water (1.0 g cm^{-3}); and ρ_P is the density of PES (1.37 g cm^{-3}).

2.10. Pure water permeability (PWP) measurement

The pure water permeability (PWP) test was conducted to evaluate the substrate hydrophilicity by measuring water flux through the substrate. All tests were performed on substrates with an effective surface area of 4.9 cm^2, using a custom-made cross-flow module. During the measurement, deionized (DI) water was used as the feed solution, and the substrate was subjected to a hydraulic pressure of 5 bar at 25 °C. The PWP value was calculated using eqn (2):

$$\mathrm{PWP} = \frac{V}{A_m \times \Delta t} \quad (2)$$

where V is the volume of permeate collected (L), A_m is the effective membrane area (m^2), and Δt is the test duration (h). Using the porosity and PWP data, the average pore radius r_p (nm) of the substrates was calculated *via* the Guerout–Elford–Ferry equation (eqn (3)):

$$r_p = \sqrt{\frac{(2.9 - 1.75\varepsilon) \times 8Q\eta T}{\varepsilon}} \quad (3)$$

The PWP value, expressed as Q (m^3 s^{-1}), represents the volumetric flow rate of the permeate and is influenced by the applied external hydraulic pressure ΔP (Pa). In the Guerout–Elford–Ferry equation, T (cm) corresponds to the substrate thickness, and η (Pa s) denotes the dynamic viscosity of water at room temperature.

2.11. Evaluation of the membrane FO performance

The FO performance of the fabricated TFC and TFN membranes was evaluated using a lab-developed cross-flow FO permeation system with an effective membrane surface area of 4.9 cm^2. Key performance parameters were measured, including water flux (J_w, LMH), reverse salt flux (J_s, gMH), and membrane selectivity (J_s/J_w), following established protocols. All tests were conducted at 25 °C using aqueous NaCl solutions at varying concentrations (0.5, 1.0, 1.5, and 2.0 M), with deionized water serving as the FS or DS depending on the test mode. The permeation cell operated at a cross-flow rate of 100 mL min^{-1}. Membrane performance

was examined in both FO mode (where the PA rejection layer faces the FS) and PRO mode (where the PA rejection layer faces the DS). Each FO test was run for approximately 30 minutes to ensure system stabilization, after which water flux and reverse salt flux data were recorded. To ensure reproducibility, each membrane was tested three times.

Water flux, J_w, was calculated by measuring the change in FS mass over time using a digital balance, according to eqn (4):

$$J_w = \frac{\frac{\Delta m_F}{\rho_F}}{A_m \times \Delta t} \quad (4)$$

where Δm_F is the change in FS mass (kg), ρ_F is the density of the FS at room temperature (kg m^{-3}), Δt is the duration of the test (s), and A_m is the effective membrane area (m^2).

Reverse salt flux, J_s, was calculated based on conductivity measurements of the FS using a conductivity meter (WTW GmbH, Germany) and according to eqn (5):

$$J_s = \frac{V_t C_t - V_0 C_0}{A_m \times \Delta t} \quad (5)$$

where V_0 and V_t are the FS volumes (L) before and after the FO test, respectively, and C_0 and C_t are the corresponding FS salt concentrations (g L^{-1}).

2.12. Evaluation of the membrane's intrinsic characteristics

Water permeability (A, LMH per bar) and salt rejection (R_s) of the as-fabricated TFC and TFN membranes were evaluated using a constant-pressure dead-end reverse osmosis (RO) permeation setup. Membrane coupons of 3.14 cm^2 were cut from each wet membrane and mounted in the RO system. DI water and 1000 ppm NaCl solution were pressurized to 5 bar across the PA active layer to determine the water permeability and salt rejection. Prior to each measurement, membranes were stabilized for 20 minutes. All experiments were conducted at 25 °C for 1 hour, with each test repeated three times using different membrane coupons. Water permeability J was calculated based on the volume of permeated DI water using eqn (6):

$$J = \frac{\Delta V}{A_m \times \Delta t \times \Delta P} \quad (6)$$

where ΔV (L) is the volume of permeate collected, A_m (m^2) is the effective membrane area, Δt (h) is the time interval, and ΔP (bar) is the applied hydraulic pressure. Salt rejection (R_s) was determined using the conductivity measurements of the feed and permeate solutions according to eqn (7):

$$R_{NaCl} = \left(1 - \frac{C_p}{C_f}\right) \times 100 \quad (7)$$

where C_f and C_p (ppm) are the salt concentrations in the feed and permeate, respectively. The salt permeability coefficient B (LMH) was calculated by fitting the rejection data into eqn (8):

$$\frac{1 - R_s}{R_s} = \frac{B}{A(\Delta P - \Delta \pi)} \quad (8)$$

where $\Delta\pi$ (bar) is the osmotic pressure difference across the membrane. Furthermore, the membrane structural parameter S (μm), which reflects internal concentration polarization, was estimated by fitting the measured A and B values to eqn (9). In this equation, π_D and π_F represent the osmotic pressures of the draw and feed solutions, respectively, and D is the salt diffusion coefficient.

$$S = \frac{D_s}{J_w} \ln \frac{A\pi_D + B}{A\pi_F + J_w + B} \quad (9)$$

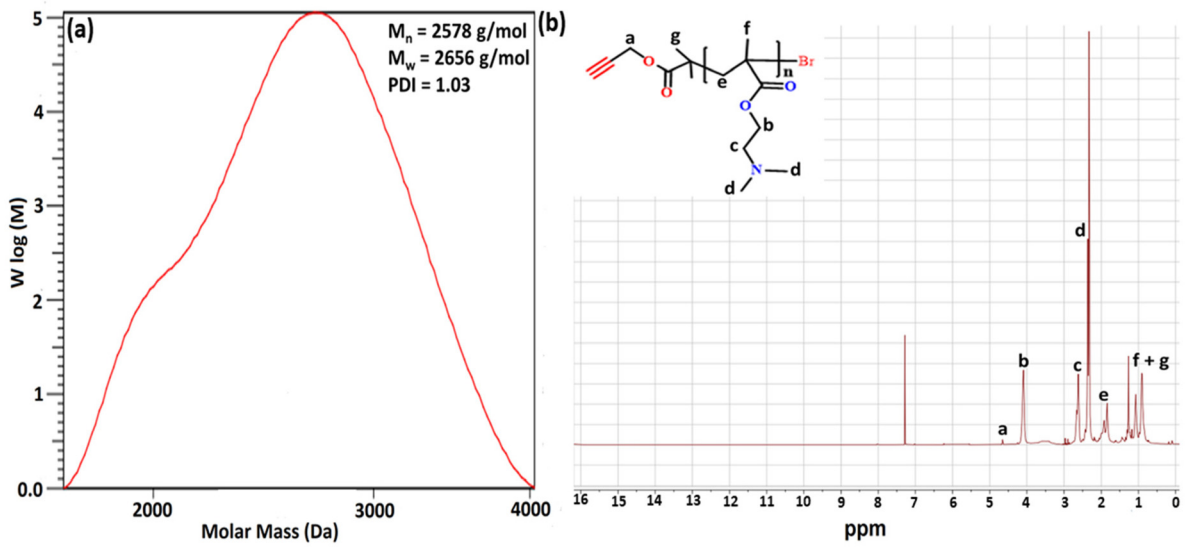

Fig. 2 (a) GPC chromatogram and (b) ^{1}H NMR spectrum of the alkynyl-terminated PDMA polymer.

3. Results and discussion

3.1. Preparation of GO-*g*-PDMA

In this study, GO-*g*-PDMA nanoplates were synthesized *via* a click reaction between alkyne-terminated PDMA and azide-functionalized GO. The overall synthetic route is illustrated in Fig. 1. Alkyne-terminated PDMA was synthesized by ATRP using PBiB as the initiator. GPC analysis of the obtained polymer (Fig. 2a) reveals a number-average molecular weight of 2578 g mol^{-1} and a weight-average molecular weight of 2656 g mol^{-1}, indicating a narrow molecular weight distribution of 1.03. The chemical structure of the synthesized PDMA was further confirmed by ^{1}H NMR spectroscopy (Fig. 2b), which shows characteristic signals corresponding to the polymer backbone and side groups. The spectrum validated successful polymerization and purification of the alkyne-terminated PDMA.

Azide-functionalized GO (GO-N_3) was synthesized in two steps. First, graphene oxide was reacted with (3-glycidyloxypropyl)trimethoxysilane (GPTMS) to introduce epoxy groups *via* silanization of the GO surface. In the second step, the epoxy-functionalized GO was reacted with sodium azide to form azide groups on the GO surface. The successful synthesis of GO-N_3 and subsequent grafting of PDMA chains onto GO *via* the click reaction were verified using several techniques including FTIR, XRD, TGA, FE-SEM and EDS analyses.

FTIR. In the FTIR spectrum of the synthesized GO *via* the modified Hummers' method, characteristic absorption peaks are observed at 3300 cm^{-1} (O–H stretching vibration), 1725 cm^{-1} (C=O stretching vibration), 1040 cm^{-1} (C–O stretching vibration), and 1615 cm^{-1} (C=C stretching in aromatic rings).[37] These typical peaks also appear in the spectra of GO-N_3 and GO-*g*-PDMA nanoplates, confirming the preservation of the fundamental GO structure after functionalization. However, their intensities decrease markedly in the GO-N_3 and GO-*g*-PDMA samples, likely due to the partial reduction of oxygenated groups during azide modification and PDMA grafting. As shown in Fig. 3a, new absorption peaks emerge at 1095 and 2090 cm^{-1} in the GO-N_3 spectrum, which correspond to the Si–O–Si stretching and azide (–N_3) stretching vibrations, respectively. These features verify the successful introduction of GPTMS and azide groups onto the GO surface. Additionally,

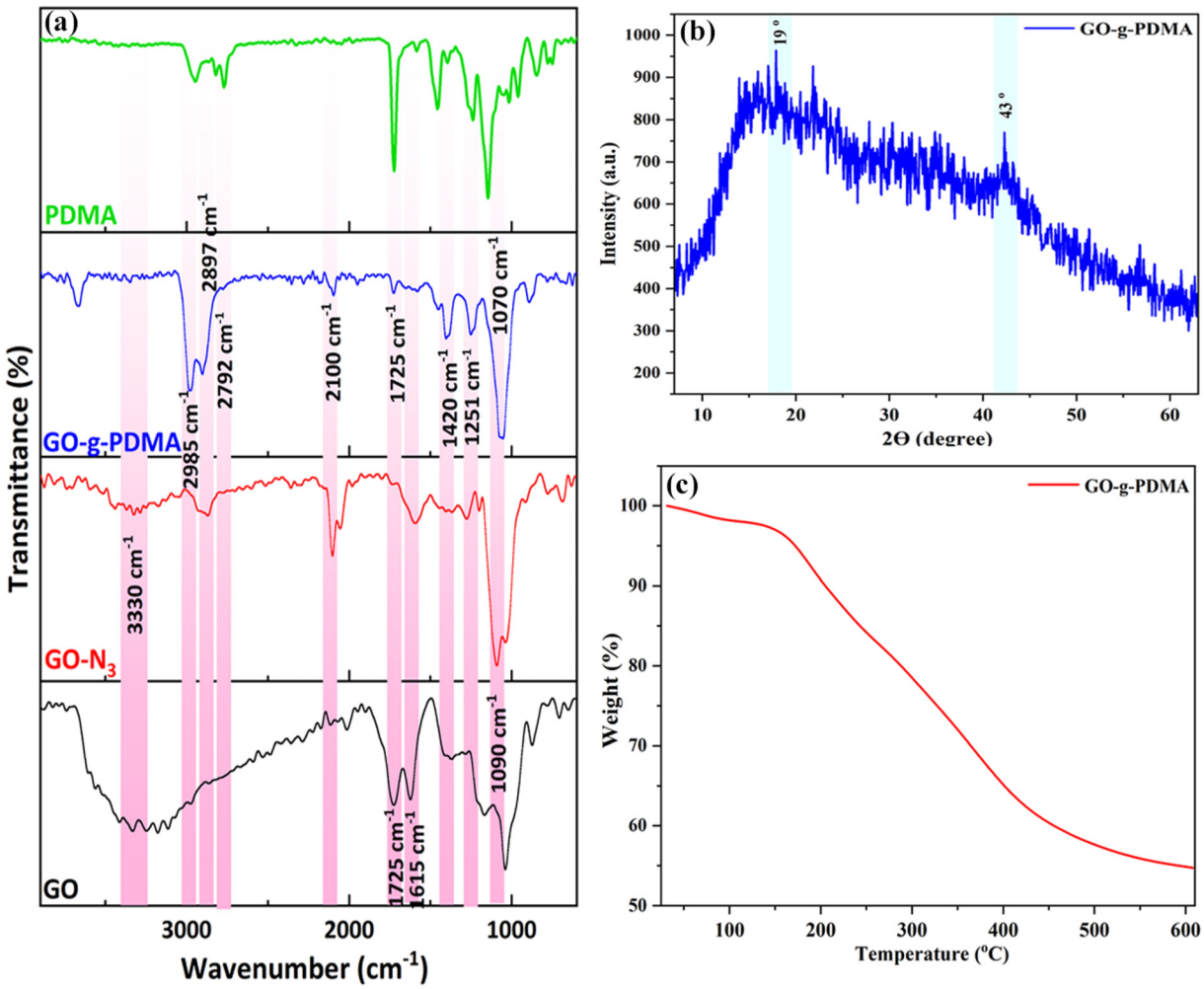

Fig. 3 (a) Comparison of FTIR spectra of the GO, GO-N_3, GO-*g*-PDMA, and PDMA polymer, (b) XRD pattern, and (c) TGA curve of the GO-*g*-PDMA.

the GO-N_3 sample shows a band at 2930 cm^{-1}, attributed to C–H stretching of the propyl chain in GPTMS. In the GO-*g*-PDMA spectrum, characteristic absorption bands arise from the grafted PDMA polymer, including C=O stretching (1725 cm^{-1}), C–N stretching of the dimethylaminoethyl group (1070 cm^{-1}), N–CH_3 stretching (2792 cm^{-1}), and C–H stretching (2985 cm^{-1}).[38] These peaks clearly confirm that the click reaction effectively grafts PDMA chains onto the GO nanoplates.

XRD. Fig. 3b displays the XRD pattern of the GO-*g*-PDMA nanoplates. According to our previous work,[31] the peak at 2θ = 9.6° corresponds to the (001) plane of oxidized graphene sheets. This peak reflects the regular interlayer spacing caused by abundant oxygen-containing functional groups, such as hydroxyl, carbonyl, epoxy, and carboxyl groups. A secondary broad and weak peak at 2θ = 43.3° is also observed and is typically attributed to residual unoxidized graphitic domains present in trace amounts within the GO structure.[39] In the case of GO-N_3, the characteristic peak at 2θ = 9.6° is retained, though its intensity is notably diminished, indicating partial disruption of the ordered GO stacking. Additionally, a broad peak at 2θ = 22.6° appears, attributed to the formation of an amorphous SiO_2 layer during GPTMS functionalization. This feature facilitates the successful chemical modification of the GO surface and the partial disruption of its crystalline structure.[40] For the GO-*g*-PDMA nanoplates, the disappearance of the GO (001) peak at 2θ = 9.6° suggests that the intercalation of PDMA chains significantly disturbs the layered GO structure. Moreover, the appearance of a broad peak around 2θ = 19° is consistent with the presence of amorphous PDMA segments, further confirming the successful grafting of the polymer onto the GO surface.[32]

TGA. TGA analysis of the GO-*g*-PDMA nanoplates was conducted under inert conditions, and the results are shown in Fig. 3c. The GO-*g*-PDMA curve was compared with the GO and GO-N_3 curves, as reported previously.[31] All samples exhibit an initial weight loss below 100 °C, which corresponds to the evaporation of physically adsorbed moisture. For the GO sample, a significant mass loss occurs around 250 °C, primarily due to the thermal decomposition of labile oxygen-containing functional groups.[41] In contrast, the GO-N_3 and GO-*g*-PDMA samples exhibit notably reduced weight loss in this temperature range, suggesting partial removal of oxygenated functionalities during functionalization with GPTMS and sodium azide, consistent with the FTIR results (Fig. 3b). The GO-N_3 sample shows a total mass loss of approximately 15.5 wt% between 300 °C and 600 °C. For the GO-*g*-PDMA nanoplates, the total weight loss in the same temperature range increases to about 24.0 wt%, indicating that the grafted PDMA polymer accounts for an estimated 8.5 wt% of the total mass.

SEM images and EDS analysis. SEM was used to examine morphological changes in GO after PDMA functionalization. As shown in Fig. 4a, pristine GO typically exhibits a crumpled, sheet-like morphology with a relatively smooth surface. The presence of oxygen-containing functional groups introduces wrinkles and folds that disrupt the intrinsic planar structure of graphene sheets.[42] Upon grafting PDMA onto the GO surface, as illustrated in Fig. 4b, a notable increase in surface roughness was observed. This appears in the SEM images as a more textured morphology, with visible protrusions and surface irregularities attributed to the presence of polymer chains. Complementary to the SEM results, EDS analysis (Fig. 4c) detected the presence of nitrogen (N) and bromine

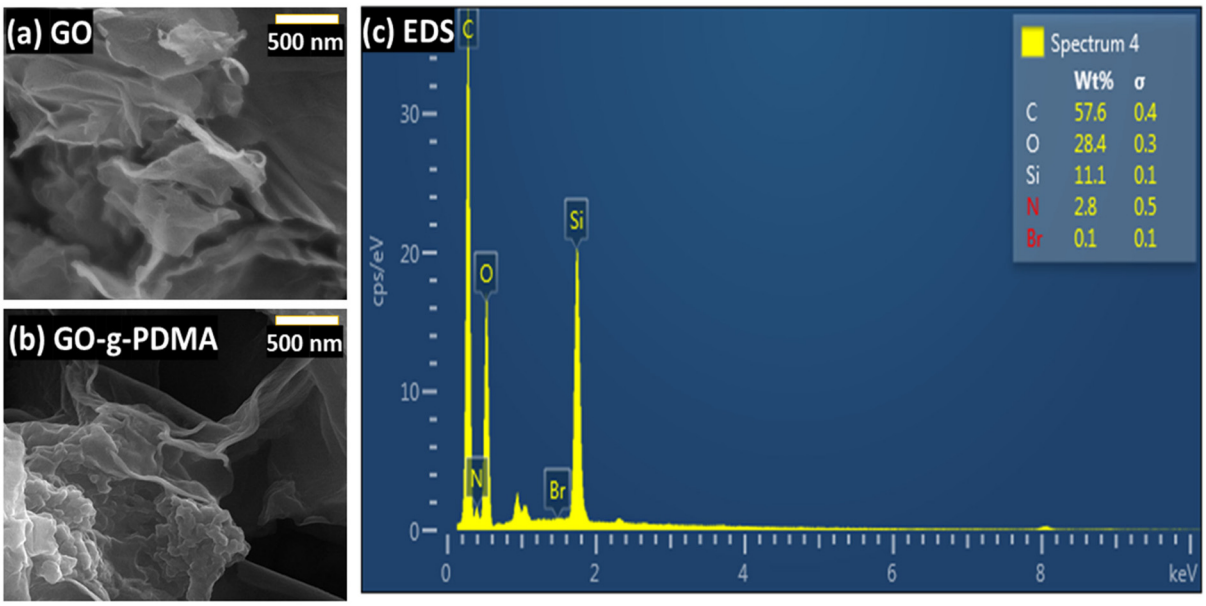

Fig. 4 SEM images of (a) GO and (b) GO-*g*-PDMA; (c) EDS spectrum of the GO-*g*-PDMA nanoplates.

(Br) in the GO-*g*-PDMA sample. These elements originate from the dimethylaminoethyl side groups of PDMA and the bromine-based ATRP initiator, respectively, and serve as supporting evidence for the successful grafting of PDMA onto the GO surface.

3.2. Substrate preparation and characterization

In this study, PES substrates were modified using GO-*g*-PDMA at three different loadings. For comparison, an additional PES substrate was prepared with unmodified GO at the same loading. A pristine PES substrate without any additives was also fabricated as a control. The preparation procedure for all substrates followed the method described in the Experimental section. The specific composition details of each formulation are summarized in Table 1.

All PES-based substrates containing GO and GO-*g*-PDMA were analyzed using ATR-FTIR spectroscopy, and the recorded spectra are shown in Fig. 5(a). The spectra of all fabricated substrates exhibit characteristic bands corresponding to the

Table 1 Compositions and labels of GO and GO-*g*-PDMA modified PES substrates and the corresponding TFN-FO membranes

Substrates	PES (g)	NMP (g)	PEG-400 (g)	Nanofiller type	Content[a] (g)	Corresponding FO membranes
PES	3.0	13.0	4.0	—	0.0	TFC
PES-$GO_{0.5}$	3.0	13.0	3.9	GO	0.1	TFN-$GO_{0.5}$
PES-$GOP_{0.25}$	3.0	13.0	3.95	GO-*g*-PDMA	0.05	TFN-$GOP_{0.25}$
PES-$GOP_{0.5}$	3.0	13.0	3.9	GO-*g*-PDMA	0.1	TFN-$GOP_{0.5}$
PES-GOP_1	3.0	13.0	3.8	GO-*g*-PDMA	0.2	TFN-GOP_1

[a] The nanofiller contents (GO or GO-*g*-PDMA) are based on the total mass of the casting solutions.

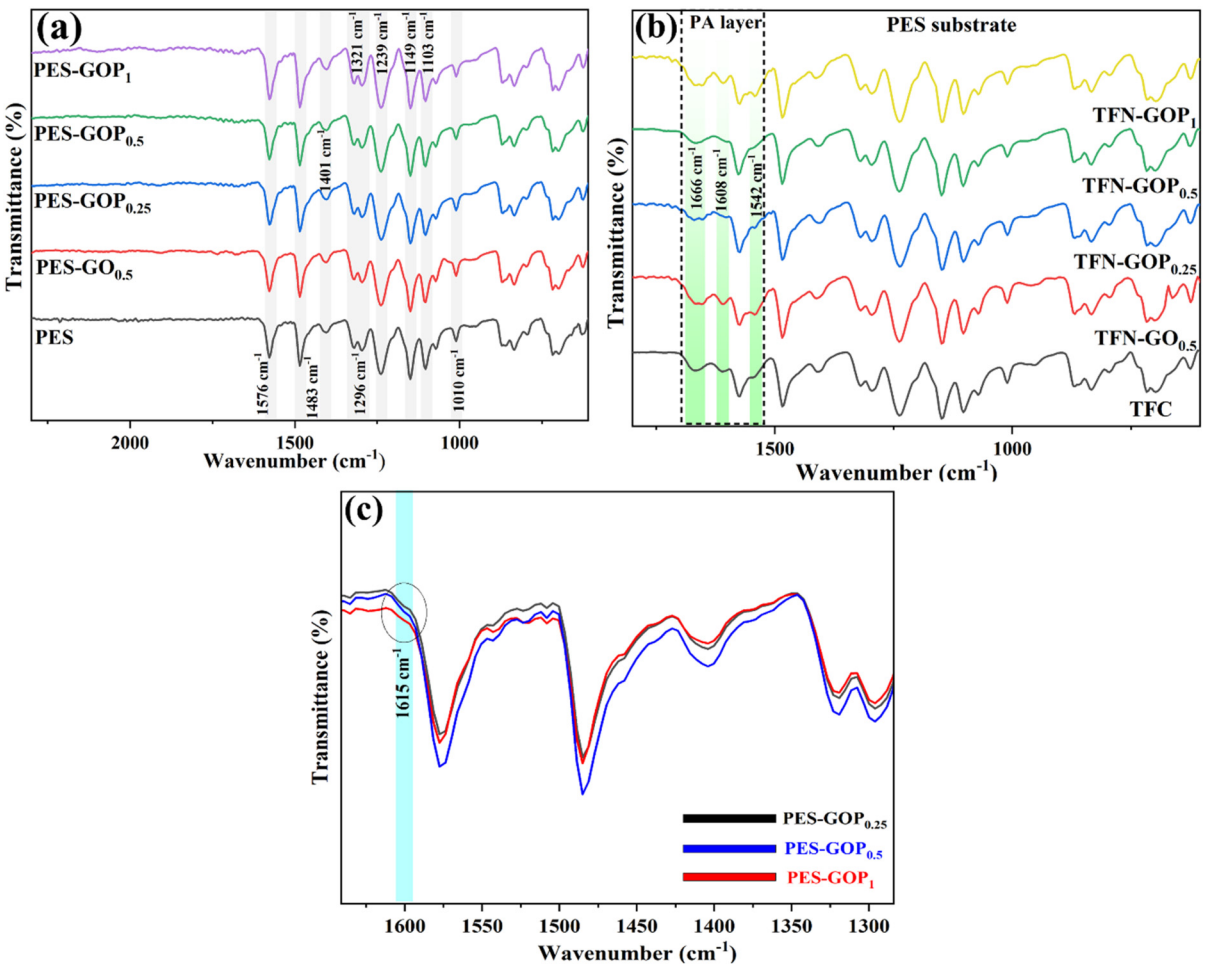

Fig. 5 ATR-FTIR spectra of (a) the prepared PES-based substrates containing GO and GO-*g*-PDMA nanofillers, (b) the fabricated TFC and TFN-FO membranes, and (c) magnification of the support layer ATR-FTIR spectra.

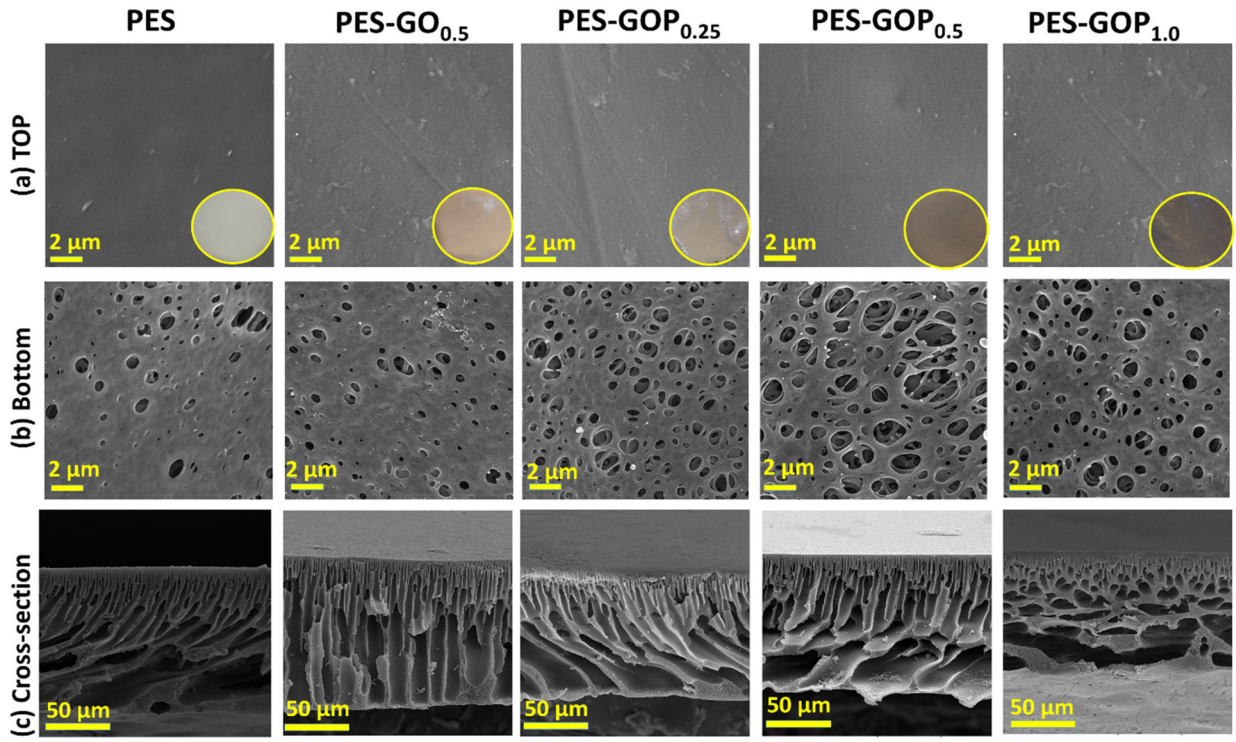

Fig. 6 (a) SEM images of the top surface morphologies and corresponding digital photographs of the substrates; (b) SEM images of the bottom surface morphologies; and (c) cross-sectional SEM images of the substrates.

PES polymer. Specifically, the bands at 1483, 1296, and 1239 cm^{-1} are attributed to the vibrations of aromatic rings, asymmetric stretching of O═S═O, and C–O–C vibrational bonding, respectively. Further analysis of the ATR-FTIR spectra of the support layers revealed that the peak at 1615 cm^{-1} became more intense as the GO-*g*-PDMA nanofiller concentration increased (Fig. 5c). This peak corresponds to the stretching vibrations of aromatic groups in the GO nanofiller. This spectroscopic finding likely explains the darker coloration of the support layers as nanofiller concentrations increase (Fig. 6a).

The effect of GO-*g*-PDMA incorporation on membrane morphology was investigated using SEM images. All substrates were fabricated using the conventional NIPS process, in which the NMP solvent in the cast polymeric film was exchanged with water (the non-solvent) to form a solid membrane. The NIPS rate critically affects the substrate structure. Most studies indicate that hydrophilic nanofillers enhance the casting solution's tolerance to water content, thereby slowing the NIPS rate.[43] Consequently, the incorporation of GO-*g*-PDMA is anticipated to substantially affect the structure of the modified PES substrates. As shown in Fig. 6a, the top surfaces of all substrates appear relatively smooth, with no visible GO or GO-*g*-PDMA nanosheets. This contrasts with membranes containing non-carbon nanofillers, such as silica[44] and TiO_2,[45] where nanofillers are typically visible on the membrane surface following the NIPS process. Similarly, other carbon-based nanofillers, such as GO-*g*-PHEMA,[31] QGO,[25] and CNTs,[46] exhibit no surface accumulation. This suggests that the carbonaceous nature of GO nanosheets and the PES polymer ensures effective dispersion of GO within the polymer matrix, preventing agglomeration on the membrane surface.[47] Additionally, the photographs in Fig. 6a illustrate that the substrate color gradually darkens with increasing nanofiller concentrations.

The morphology of the bottom surface of FO membranes directly influences water and solute diffusion through the substrate pores, so it is essential to analyze the structural changes that occur when hydrophilic nanofillers are added. Fig. 6(b) presents SEM images of the bottom surfaces of all substrates, revealing significant morphological modifications. The pore sizes on the bottom side of GO or GO-*g*-PDMA-modified substrates are considerably larger than those of the unmodified substrate. This variation in pore size can be attributed mainly to two factors: (1) the interfacial affinity between the glass plate and the casting solution, and (2) the interval between gelation initiation and film detachment.[48] Since a porous substrate helps mitigate ICP, it is reasonable to expect that the modified substrates will exhibit enhanced performance in FO processes.

Cross-sectional SEM images provide further insights into the impact of nanofillers on substrate morphology. As shown in Fig. 6c, all substrates exhibit two distinct regions: a dense top layer and a porous bottom layer, characteristic of membranes formed *via* the NIPS process.[49] The unmodified PES substrate exhibits irregular pore structures in the cross-section, resulting from rapid solvent–nonsolvent (NMP–water)

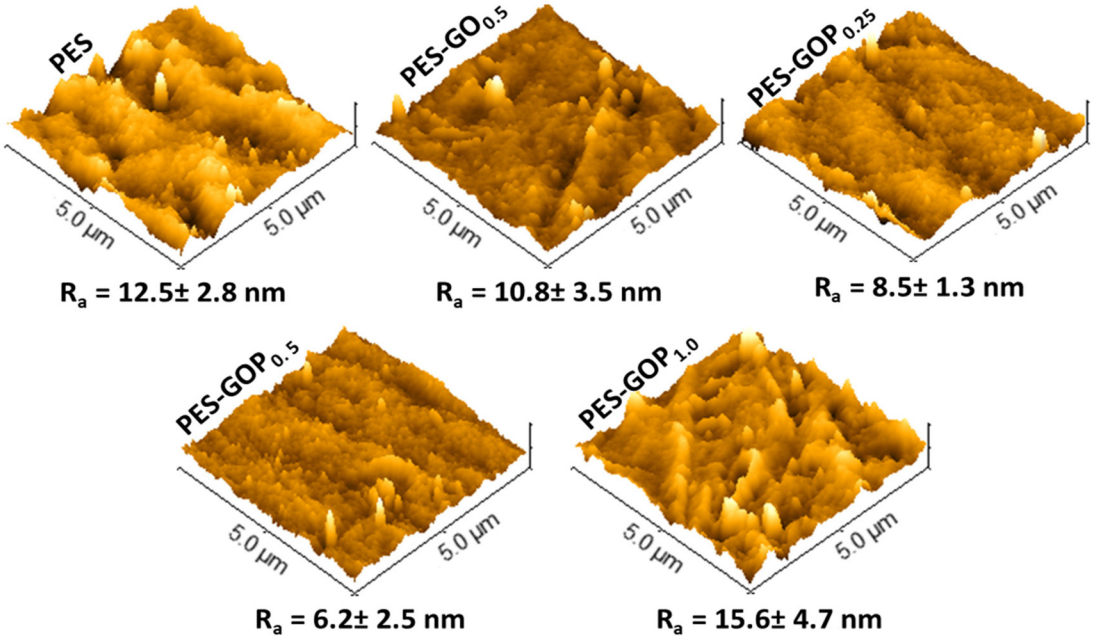

Fig. 7 Three-dimensional AFM images of PES substrates modified with GO and GO-*g*-PDMA nanofillers, showing variations in surface roughness.

exchange during phase inversion, driven by PES's intrinsic hydrophobicity.[50] In contrast, substrates modified with GO or GO-*g*-PDMA demonstrate significantly larger and more uniform pores throughout the cross-section. Increasing the GO-*g*-PDMA content encourages the creation of elongated finger-like pores, probably because the hydrophilic groups in GO and GO-*g*-PDMA reduce the solvent–nonsolvent exchange rate during NIPS, thereby promoting pore formation. However, at a higher GO-*g*-PDMA concentration of 1.0 wt%, the morphology shifts from finger-like to sponge-like, accompanied by a decrease in porosity. This change is likely due to the aggregation of GO-*g*-PDMA nanosheets at elevated loadings, which reduces their ability to effectively influence the phase inversion process.

In addition to influencing morphology, nanofillers also affect the surface roughness of membranes. Fig. 7 shows three-dimensional surface images of PES, PES-GO$_{0.5}$, PES-GOP$_{0.25}$, PES-GOP$_{0.5}$, and PES-GOP$_1$ substrates. The average surface roughness (R_a, nm) values are reported alongside the images. The pure PES substrate exhibits a relatively rough surface, with an R_a value of 12.5 ± 2.8 nm, which is higher than that of the GO and GO-*g*-PDMA-modified PES substrates. This reduction in roughness is likely due to the hydrophilic nanofillers at the surface, which contribute to a more controlled NIPS process and result in smoother membranes. However, at the highest nanofiller loading in PES-GOP$_1$, the R_a value increases again to an approximate value similar to that of bare PES. This increase could be due to nanofiller agglomeration, which decreases the uniformity of nanofiller coverage on the substrate surface and consequently impacts roughness.

The addition of nanofillers to the PES substrate also alters the intrinsic membrane properties, such as porosity, mean pore size, hydrophilicity, and pure water permeability (PWP). The porosity of the substrates is measured using the gravimetric method, and the results are shown in Fig. 8a. Increasing the GO-*g*-PDMA loading from 0 to 0.5 wt% significantly enhances the porosity of the PES matrix, increasing it from 74.4 ± 1.5% to 82.6 ± 1.1%. This increase in porosity can be attributed to several mechanisms: (1) the intercalation of GO-*g*-PDMA nanosheets into the PES polymer chains, which causes structural modification of the matrix, and (2) the inherent hydrophilicity of GO-*g*-PDMA nanosheets, which improves the overall hydrophilicity of the casting solution, affecting NIPS during substrate formation and resulting in a more porous structure.[43] However, when the GO-*g*-PDMA loading exceeds the optimal 0.5 wt% and reaches 1.0 wt%, a slight decrease in porosity is observed (78.4 ± 1.2%). This reduction likely results from increased viscosity of the casting solution, which affects the NIPS process, and from potential pore blockage due to excessive nanosheet aggregation. To further assess the effect of PDMA grafting on porosity enhancement, pristine GO nanosheets are also incorporated into the PES matrix at 0.5 wt%. The resulting porosity for the PES-GO$_{0.5}$ sample (78.03%) is higher than that of the pure PES substrate but lower than that of the PES-GOP$_{0.5}$ substrate. This result suggests that polymer grafting on the GO surface significantly improves the nanofiller's ability to enhance porosity. The presence of grafted PDMA chains improves compatibility between the GO nanosheets and the PES matrix, thereby minimizing aggregation and promoting a more uniform dispersion throughout the substrate.

In addition to porosity, Fig. 8a also shows the WCA measurements of the substrates, which serve as an indicator of surface hydrophilicity. The hydrophilicity of a substrate plays a

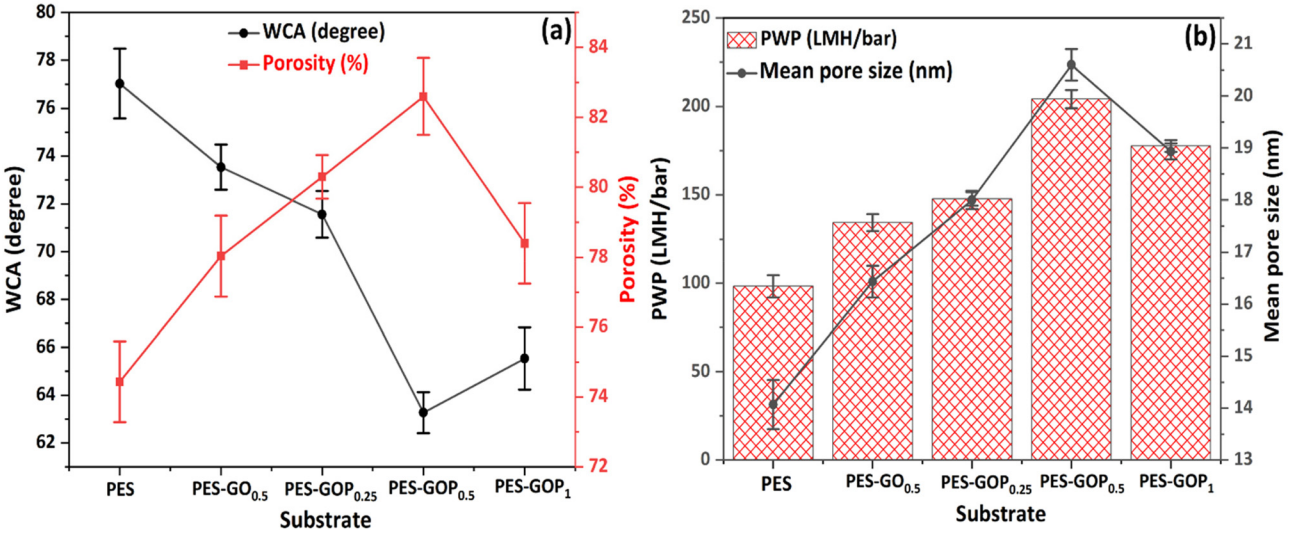

Fig. 8 (a) Porosity and water contact angle of unmodified and nanofiller-modified PES substrates. (b) Pure water permeability and mean pore size of the corresponding substrates.

crucial role in determining water flux. For the PES-$GO_{0.5}$ substrate, the presence of oxygen-containing functional groups in GO nanosheets reduces the WCA to 73.5° ± 0.94. A more pronounced decrease in WCA is observed when GO-*g*-PDMA nanosheets are incorporated, particularly up to 0.5 wt%, indicating a substantial improvement in surface hydrophilicity. Specifically, the WCA of the unmodified PES substrate was recorded as 77.0° ± 1.45, which decreased to 63.2° ± 0.86 in the PES-$GOP_{0.5}$ substrate. This reduction is mainly due to the inherent hydrophilicity of GO-*g*-PDMA nanosheets, which is provided by the polar functional groups in the PDMA chains. PDMA possesses tertiary amine groups (–$N(CH_3)_2$) and ester groups (–COO), which can form strong dipole–dipole interactions with water molecules, thereby improving the wettability of the substrate surface. Notably, the WCA decrease is more substantial in the PES-$GOP_{0.5}$ sample than in the PES-$GO_{0.5}$ sample, which contains unmodified GO. This enhanced hydrophilicity is attributed to improved compatibility between the GO nanosheets and the PES matrix resulting from PDMA grafting.[51] The polymeric modification enhances nanosheet dispersion and reduces aggregation, resulting in a more homogeneously hydrophilic surface and improved overall membrane performance.

The mean pore size and PWP are other key substrate properties influenced by the nanofillers. The pore size trend is similar to the porosity trend, which shows that by increasing the nanofiller content, both porosity and mean pore size are enhanced simultaneously. As shown in Fig. 8b, the PWP of the PES-$GO_{0.5}$ substrate reaches 134.4 ± 4.7 LMH per bar, representing an increase of approximately 36% compared to the unmodified PES substrate (98.3 ± 6.3 LMH per bar). Remarkably, the PES-$GOP_{0.5}$ substrate exhibits the highest PWP value of 204.1 ± 5.2 LMH per bar, more than twice that of the pristine PES. Several mechanisms contribute to this enhancement in permeability: (1) increased porosity facilitates more efficient water transport through the membrane matrix, (2) enhanced surface hydrophilicity promotes water adsorption and diffusion, (3) the formation of well-developed finger-like pores optimizes water flow pathways; and (4) the GO-*g*-PDMA nanofillers function as hydrophilic nanochannels, enabling additional water transport routes.[52]

3.3. Influence of substrate modification on the PA active layer

The PA active layer in TFC-FO membranes is responsible for selective water transport while rejecting solutes. In this study, all PA layers were fabricated using the same IP method on different PES-based substrates. However, notable variations in the structure and properties of the PA layers were observed depending on the substrate. As with the substrates, the TFC and TFN membranes were characterized using ATR-FTIR spectroscopy. Because the ATR-FTIR beam penetration depth was approximately 1 μm and the thickness of the PA layer was about 400 nm, characteristic peaks from the substrates were also detectable. Nonetheless, all TFN membranes display distinct peaks at 1540 cm^{-1}, 1610 cm^{-1}, and 1660 cm^{-1}, which correspond to N–H in-plane bending (amide II), C=C aromatic ring stretching, and C=O stretching (amide I), respectively.[53] The presence of these peaks confirms the successful formation of the PA selective layer.

In general, the morphology of the PA layer changes depending on the substrate, as shown in Fig. 9a. The formation of the PA layer generally proceeds through two stages: initially, MPD reacts with TMC at the water-organic interface to form an ultrathin, nodular PA layer. Then, the Marangoni effect enhances the transport of MPD toward the organic phase, restructuring the nascent layer into a characteristic ridge-and-valley morphology. On the unmodified PES substrate (TFC), the PA layer

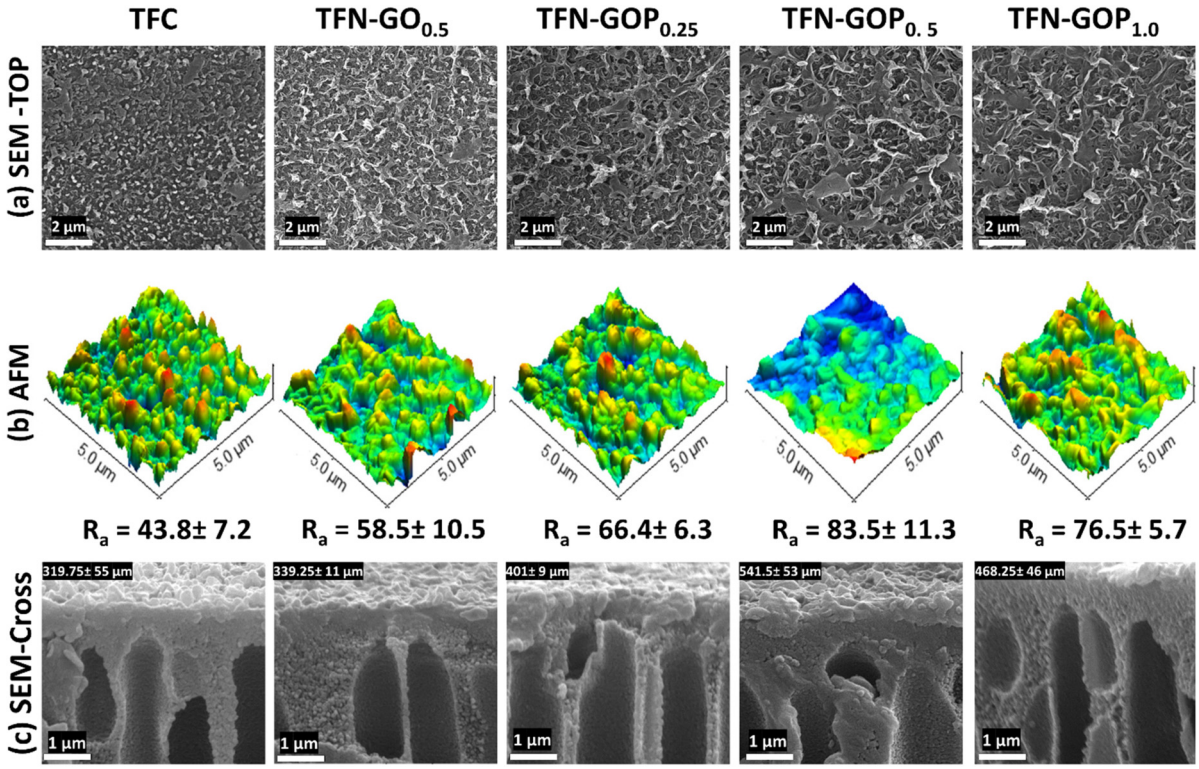

Fig. 9 (a) Top surface SEM images showing the morphological differences in the PA layers of TFC and TFN-FO membranes; (b) three-dimensional AFM images depicting changes in surface roughness with increasing GO-*g*-PDMA content; and (c) cross-sectional SEM images illustrating the overall membrane structure and thickness of the PA layers formed on different substrates.

appears the smoothest, with a relatively uniform nodular morphology. This is attributed to the limited adsorption of MPD onto the hydrophobic, low-porosity PES surface.[19] In contrast, as the GO-*g*-PDMA content in the substrate increases, the PA layer develops a rougher, more textured surface. This transformation is primarily due to the improved hydrophilicity and porosity of the modified substrates, which enable greater absorption of the MPD solution and result in a more vigorous interfacial polymerization reaction. A rougher PA surface increases the effective surface area available for water transport. This trend is supported by AFM analysis shown in Fig. 9b, where the average surface roughness (R_a) increases from 43.8 ± 7.2 nm for the TFC membrane to 83.5 ± 11.3 nm for TFN-GOP$_{0.5}$. These findings confirm that variations in substrate wettability and porosity strongly influence the morphology of the resulting PA layer.[54]

In addition to surface morphology and roughness, the thickness of the PA layer is a critical factor influencing the water permeability and solute rejection performance of TFN-FO membranes. Notably, the trend in PA layer thickness correlates closely with changes in surface roughness. The measured thicknesses of the PA layers for TFC, TFN-GO$_{0.5}$, TFN-GOP$_{0.25}$, TFN-GOP$_{0.5}$, and TFN-GOP$_1$ membranes are 319.75 ± 55, 339.25 ± 11, 401 ± 9, 541.5 ± 53, and 468.25 ± 46 nm, respectively. The observed increase in PA thickness is attributed to several factors, including enlarged surface pore size of the substrates, enhanced absorption of MPD monomers into the substrate surface pores, and an accelerated IP reaction[45]. These factors promote the formation of a thicker and more developed PA layer, which can influence membrane separation properties. The cross-sectional images of the TFN membranes were further analyzed to investigate the distribution of GO-*g*-PDMA within the PES substrate. Fig. 10 shows the elemental mapping results for the TFN-GOP$_{0.5}$ sample, highlighting the uniform distribution of carbon, nitrogen, sulfur, oxygen, and silicon across the membrane cross-section. Notably, the presence of silicon and nitrogen, originating from the GPTMS moieties introduced during the azide-functionalization of GO nanosheets, serves as distinctive markers, differentiating the GO-*g*-PDMA nanofiller from the intrinsic elements of the PES substrate. The uniform distribution of these elements throughout the membrane cross-section indicates uniform dispersion of the GO-*g*-PDMA nanofiller and suggests a high degree of compatibility between the functionalized nanofiller and the PES matrix.

3.4. Evaluation of intrinsic separation performance

The intrinsic separation characteristics of the TFC and TFN-FO membranes, including water permeability (A), salt permeability coefficient (B), salt rejection (R), the B/A ratio, and the membrane structural parameter (S value), are critical for determining membrane performance in FO applications.

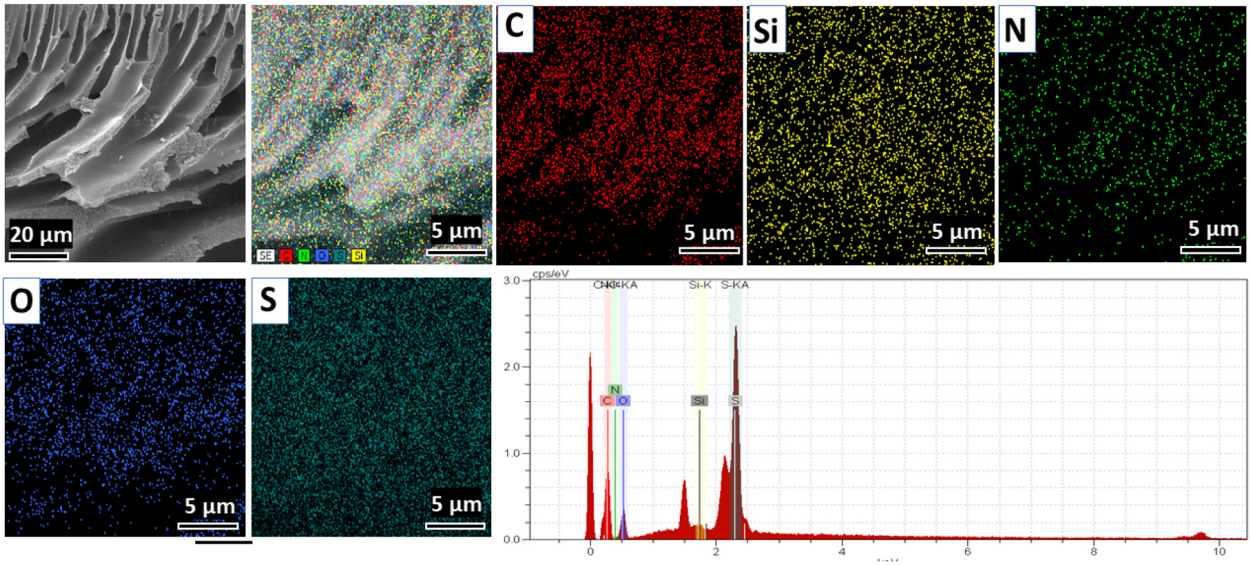

Fig. 10 EDS elemental mapping images of the TFN-$GOP_{0.5}$ membrane.

Table 2 Intrinsic transport parameters of TFC and TFN-FO membranes evaluated under RO mode: water permeability (*A*), salt permeability (*B*), salt rejection (*R*), selectivity ratio (*B*/*A*), and structural parameter (*S*)

FO membranes	*A* (LMH per bar)	*R* (%)	*B* (LMH)	*B*/*A* (bar)	*S* (μm)
TFC	1.22 ± 0.06	94.4 ± 0.6	0.30 ± 0.04	0.25 ± 0.03	579 ± 40
TFN-$GO_{0.5}$	1.63 ± 0.10	93.8 ± 0.35	0.45 ± 0.03	0.27 ± 0.015	442 ± 73
TFN-$GOP_{0.25}$	1.97 ± 0.1	95.1 ± 0.3	0.42 ± 0.05	0.21 ± 0.015	385 ± 29
TFN-$GOP_{0.5}$	2.53 ± 0.09	96.3 ± 0.45	0.41 ± 0.07	0.16 ± 0.02	270 ± 26
TFN-GOP_1	2.47 ± 0.18	91.03 ± 0.61	1.04 ± 0.15	0.42 ± 0.03	350 ± 42

These parameters are measured for each membrane and are summarized in Table 2. Both GO and GO-*g*-PDMA-modified TFN-FO membranes demonstrate higher *A* values than the unmodified TFC membrane, indicating enhanced water permeability. In particular, increasing the GO-*g*-PDMA content led to a notable increase in *A* value, which corresponds with the formation of a rougher PA active layer, as confirmed by SEM and AFM analyses. A rougher PA surface increases the effective contact area with water, thereby improving water permeability. The *R* values vary with the type and concentration of the nanofiller. The TFN-$GO_{0.5}$ membrane exhibits a slightly reduced *R* value (93.8 ± 0.35%) compared to the TFC membrane (94.4 ± 0.6%). In contrast, the TFN-$GOP_{0.5}$ membrane shows an improved *R* value, attributed to a uniform, well-formed PA rejection layer resulting from optimal nanofiller distribution. However, further increasing the GO-*g*-PDMA content to 1.0 wt% (TFN-GOP_1) results in a reduced *R* value (91.03 ± 0.61%), likely due to defective PA layer formation caused by nanofiller aggregation at higher concentrations. The salt permeability coefficient (*B*), calculated from *A* and *R* values, followed a similar trend, initially decreasing with moderate GO-*g*-PDMA content and increasing at higher loading levels. These trends in *A*, *B*, and *R* values highlight the role of GO-*g*-PDMA in improving water permeability and selectivity when uniformly dispersed but in causing performance deterioration at high loading. The *S* value, which characterizes the ICP effect, is also evaluated using data from RO and FO tests. A lower *S* value indicates diminished ICP and improved FO flux.[55,56] The unmodified TFC membrane exhibited the highest *S* value (579 ± 40 μm) and the lowest FO flux. In contrast, TFN-$GOP_{0.5}$ shows the lowest *S* value (270 ± 26 μm), corresponding to the highest FO flux. These results suggest that the addition of GO-*g*-PDMA nanosheets effectively reduces the ICP effect, improving overall FO membrane performance.

3.5. FO performance

The FO performance of the TFC and GO-*g*-PDMA-modified TFN membranes was evaluated using a cross-flow permeation cell under both FO and PRO modes. The results, including water flux (J_w), reverse salt flux (J_s), and specific reverse salt flux (J_s/J_w), are shown in Fig. 11. The unmodified TFC membrane exhibited J_w values of 13.12 ± 0.82 LMH and 21.55 ± 1.2 LMH under FO and PRO modes, respectively. The incorporation of GO-*g*-PDMA nanosheets into the PES substrate led to a marked enhancement in water flux with increasing nanofiller content from 0.25 to 0.5 wt%. For instance, the J_w values for the TFN-$GO_{0.5}$, TFN-$GOP_{0.25}$, and TFN-$GOP_{0.5}$ membranes increased to 17.3 ± 1.45/31.09 ± 1.2 LMH, 20.27 ± 0.83/38.58 ± 1.3 LMH, and 27.82 ± 1.96/52.1 ± 1.4 LMH under FO/PRO modes, respectively. This enhancement in FO performance is primarily attributed to the introduction of hydrophilic GO-*g*-PDMA nanosheets into the membrane matrix. These nanofillers improve the substrate's average pore size and overall poro-

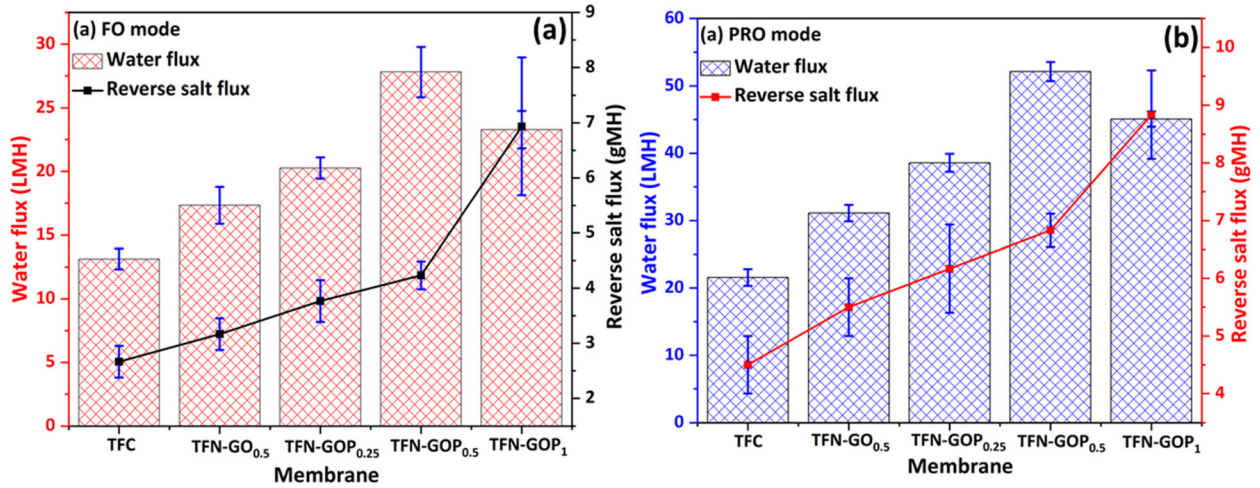

Fig. 11 Water flux (J_w) and reverse salt flux (J_s) of TFC and GO/GO-*g*-PDMA-modified TFN-FO membranes in (a) FO mode and (b) PRO mode. Tests are performed using a 1 M NaCl draw solution and DI water as the feed.

sity, while promoting the formation of elongated finger-like structures. Additionally, the nanosheets significantly enhance membrane hydrophilicity, as evidenced by reduced water contact angles. These morphological and surface improvements synergistically enhance water transport across the membrane.[57,58] In addition to the favorable structural features of the substrate, the increased roughness of the PA active layer also contributes to the improved water flux observed in the GO-*g*-PDMA-blended TFN-FO membranes. A rougher PA layer provides a larger effective contact area for interaction with water molecules, thereby enhancing permeability. Consequently, the improved water flux can be attributed to the synergistic effects of enhancements in both the substrate structure and the PA active layer morphology. The FO performance data also reveal that the J_w values in PRO mode are consistently higher than those in FO mode for all membrane samples. This trend aligns with a well-established principle in FO processes, where PRO mode generally experiences reduced ICP effect compared to FO mode.[59] However, in the TFN-GOP$_1$ sample, a slight reduction in J_w is observed due to the nanofiller's non-uniform dispersion at higher concentrations. Specifically, increasing the nanofiller content increases the viscosity of the casting solution, which can alter membrane morphology, leading to the formation of a sponge-like substrate structure with less favorable water-transport characteristics.

In addition to water flux (J_w), the reverse salt flux (J_s) is a critical parameter that significantly influences the overall efficiency and selectivity of membranes in the FO process. Fig. 11a and b illustrate the J_s trends for both TFC and TFN membranes modified with GO or GO-*g*-PDMA over a concentration range of 0–1.0 wt% under FO and PRO operation modes. With increasing GO-*g*-PDMA content, J_s values gradually increased, reaching their maximum at a nanofiller loading of 1.0 wt%. Specifically, J_s increased from 2.6 ± 0.28/4.5 ± 0.5 gMH for the unmodified TFC membrane to 6.9 ± 1.25/8.83 ± 0.76 gMH for the TFN-GOP$_1$ membrane under FO/PRO modes, respectively. This elevated J_s in TFN-GOP$_1$ aligns with the observed trends in salt permeability (B) and salt rejection (R) values, suggesting defective PA layer formation at high filler loading. Nonetheless, the J_s values for all GO and GO-*g*-PDMA-modified TFN membranes remain relatively low and are below those typically reported for many conventional TFC-FO membranes in the literature, indicating a favorable balance between permeability and selectivity.

Moreover, membrane selectivity, defined by the ratio of reverse salt flux to water flux (J_s/J_w), is a key metric for evaluating FO membrane performance. High selectivity, indicated by a low J_s/J_w value, is essential in applications such as desalination, water treatment, and resource recovery, as it ensures efficient water transport while minimizing solute leakage. A major challenge in FO membrane design is overcoming the inherent trade-off between water permeability and salt rejection. As depicted in Fig. 12a, the TFN-GOP$_{0.5}$ membrane, which incorporates 0.5 wt% GO-*g*-PDMA nanofiller exhibited the lowest J_s/J_w ratios of 0.15 (FO mode) and 0.13 (PRO mode), indicating superior selectivity. However, this ratio increased sharply when the nanofiller content was raised to 1.0 wt%, reflecting diminished performance, likely due to nanofiller aggregation or non-uniform distribution. These findings highlight that the TFN-GOP$_{0.5}$ membrane achieves an optimal balance between high water permeability and low reverse salt diffusion, making it a promising candidate for high-performance FO applications.

To evaluate the FO performance of the optimal TFN-GOP$_{0.5}$ membrane, the influence of varying DS concentrations (0.5, 1.0, 1.5, and 2.0 M NaCl) on water flux is investigated and compared with the unmodified TFC membrane, as shown in Fig. 12(b). In both membranes, J_w increases with increasing DS concentration, attributable to the corresponding increase in osmotic pressure, which drives water transport in the FO process.[60] However, the TFN-GOP$_{0.5}$ membrane shows a much sharper increase in J_w compared to the unmodified TFC mem-

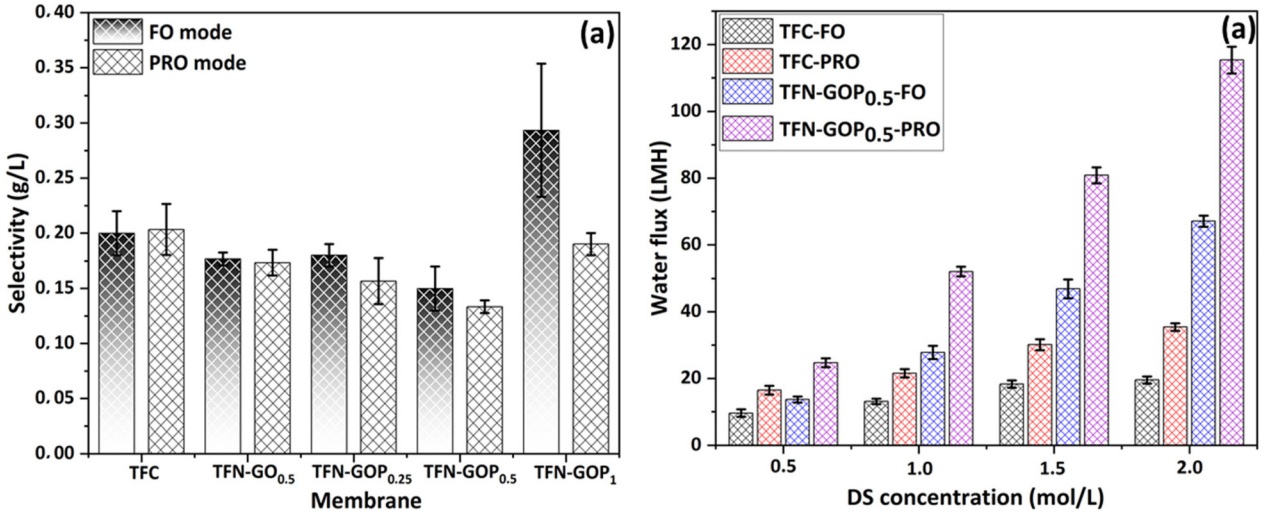

Fig. 12 (a) Selectivity (J_s/J_w) of the TFC and TFN-FO membranes in FO and PRO modes. (b) Effect of DS concentration on the water flux of TFC and TFN-$GOP_{0.5}$ membranes.

brane. For example, as the DS concentration increased from 0.5 to 2.0 M, the TFC membrane showed increases in J_w of approximately 103% and 114.5% under FO and PRO modes, respectively. In contrast, the TFN-$GOP_{0.5}$ membrane shows a remarkable increase of approximately 393.4% and 366% under the same conditions. This pronounced enhancement is attributed to the improved structural properties of the GO-*g*-PDMA-modified substrate, including enhanced hydrophilicity, increased porosity, and a more favorable finger-like pore morphology. These features help mitigate the ICP effect, particularly at higher DS concentrations, thereby sustaining higher water flux.

Stability of GO-*g*-PDMA in the TFN-FO membranes. The long-term stability of hydrophilic nanofillers within the membrane matrix is essential for preserving membrane performance, structural integrity, and resistance to environmental stress during FO operations. To evaluate the stability of GO-*g*-PDMA nanosheets in the PES substrate, UV-vis spectrophotometry is employed. The TFN-$GOP_{0.5}$ membrane was immersed in DI water under agitation for 30 days. After this period, the water was analyzed to detect any leached GO-*g*-PDMA. The UV-vis spectrum shows no characteristic absorption peaks for GO-*g*-PDMA, indicating no leaching. This result confirms the strong compatibility and stable incorporation of GO-*g*-PDMA within the PES matrix, supporting its potential for long-term use in FO membranes without compromising structural integrity or performance.

To demonstrate stability, we also evaluated water flux, reverse salt flux, water permeability coefficient, and salt rejection rate of the optimized TFN-$GOP_{0.5}$ membrane. After storage in DI water for 6 months, its performance was tested in FO and RO systems. Results showed that even after six months, the water flux and reverse salt flux of the TFN-$GOP_{0.5}$ membrane remained almost unchanged. Likewise, the water permeability coefficient and salt rejection rate exhibited no significant change. This indicates that the GO-*g*-PDMA nanofiller has excellent stability within the support layer.

To give a clearer view of how GO-*g*-PDMA nanosheets affect the membrane substrate, a comparison table (Table 3) has been prepared. This table compares the osmotic performance para-

Table 3 Comparison of the FO performance of the TFC and TFN-$GOP_{0.5}$ membranes developed in this study with other GO-based FO membranes reported in the literature

Membrane code	TFC	TFN-$GOP_{0.5}$	TFN-$GP_{21}^{0.4}$	TFC M_2	CN/rGO-M-0.5	TFN-2	TFN-GO
Substrate	PES	PES	PSf	PSf	PES	PSf	PSf
J_w (LMH)	13.0	27.8	15.6	21.3	32.5	13.4	9.2
Selectivity (g L^{-1})		0.15	0.1	0.23	0.22	0.46	0.41
J_w improvement (%)	—	112	165	130	30	55.8	7.0
Modifiers	No filler		GO-*g*-PHEMA	GO-CS	rGO/C_3N_4	LDH/GO	GO
Weight ratio (wt%)	—	0.5	0.4	0.5	0.5	2.0	2.0
S value (μm)	579	270	710.8	484	163	138	—
Test conditions DS/FS	1.0 M NaCl/DI-water	1.0 M NaCl/DI-water	1.0 M NaCl/DI-water	1.0 M NaCl/DI-water	1.0 M NaCl/DI-water	1.0 M NaCl/DI-water	1.0 M NaCl/DI-water
Ref.	This work	This work	[31]	[33]	[61]	[62]	[23]

meters of the FO membranes developed in this study (TFC and TFN-GOP$_{0.5}$) with those reported for other GO-based FO membranes in the literature. Additionally, the percentage improvement in J_w relative to the unmodified TFC membrane is shown to quantify the performance enhancement. Among the membranes evaluated, the TFN-GOP$_{0.5}$ membrane demonstrates the most favorable combination of high water flux, low reverse salt flux, and superior selectivity, highlighting its competitiveness and optimal design relative to other GO-modified FO membranes.

4. Conclusion

This study demonstrates the development and optimization of a high-performance TFN-FO membrane incorporating GO-*g*-PDMA nanosheets. The functionalization of GO with PDMA *via* click chemistry is confirmed using FTIR, XRD, TGA, SEM, and EDS analyses. Embedding GO-*g*-PDMA into the PES substrate significantly enhances its structural and physicochemical properties. At an optimal loading of 0.5 wt%, the modified substrate exhibits increased porosity (82.6 ± 1.1%), improved hydrophilicity (WCA: 63.2 ± 0.86°), and elevated pure water permeability (204.1 ± 5.2 LMH per bar). These enhancements are attributed to the synergistic effects of uniform nanofiller dispersion, greater surface wettability, and the formation of an optimized finger-like pore structure. These improvements effectively reduced ICP, as shown by the lower structural parameter (S = 270 ± 26 μm) of the TFN-GOP$_{0.5}$ membrane, thus enhancing overall FO performance. The interfacial polymerization on the modified substrate formed a PA active layer with increased surface roughness (R_a = 83.5 ± 11.3 nm) and thickness (541.5 ± 53 nm), which enhanced the effective surface area for water transport while maintaining high salt rejection. In FO and PRO modes, the TFN-GOP$_{0.5}$ membrane achieves water fluxes of 27.82 ± 1.96 LMH and 52.1 ± 1.4 LMH, respectively, using a 1.0 M NaCl draw solution, representing a 124% and 100% increase, respectively, over the unmodified TFC membrane. Notably, the TFN-GOP$_{0.5}$ membrane also exhibits superior selectivity (low J_s/J_w ratio), outperforming other GO-based FO membranes reported in the literature. However, excessive loading of GO-*g*-PDMA (1.0 wt%) led to nanofiller aggregation, reduced porosity, and compromised PA layer formation, highlighting the critical importance of optimizing nanofiller concentration. Overall, incorporating GO-*g*-PDMA nanosheets offers a promising strategy to simultaneously address ICP limitations and enhance both water permeability and membrane selectivity.

Conflicts of interest

There are no conflicts to declare.

Data availability

All data supporting the findings of this study are included in the article.

No additional datasets, software, or code were generated or analyzed during this study.

Acknowledgements

This research was funded by the German Federal Ministry of Science and Education in the framework of the MEWAC program under the HydroDeSal project (Project Code 02WME1613).

References

1 G. O. R. e Silva, C. R. dos Santos, G. S. Casella, G. P. Drumond and M. C. S. Amaral, Membrane fouling in integrated forward osmosis and membrane distillation systems–a review, *Sep. Purif. Technol.*, 2025, **356**, 129955, DOI: 10.1016/j.seppur.2024.129955.
2 M. Elimelech and W. A. Phillip, The future of seawater desalination: Energy, technology, and the environment, *Science*, 2011, **333**, 712–717, DOI: 10.1126/SCIENCE.1200488.
3 W. Xu, Q. Chen and Q. Ge, Recent advances in forward osmosis (FO) membrane: Chemical modifications on membranes for FO processes, *Desalination*, 2017, **419**, 101–116, DOI: 10.1016/J.DESAL.2017.06.007.
4 M. Joafshan, A. Shakeri, S. R. Razavi and H. Salehi, Gas responsive magnetic nanoparticle as novel draw agent for removal of Rhodamine B via forward osmosis: High water flux and easy regeneration, *Sep. Purif. Technol.*, 2022, **282**, 119998, DOI: 10.1016/J.SEPPUR.2021.119998.
5 A. Shakeri, S. M. M. Babaheydari, H. Salehi and S. R. Razavi, Reduction of the Structure Parameter of Forward Osmosis Membranes by Using Sodium Bicarbonate as Pore-Forming Agent, *Langmuir*, 2021, **37**(24), 7591–7599, DOI: 10.1021/acs.langmuir.1c01097.
6 V. Sant'Anna, L. D. F. Marczak and I. C. Tessaro, Membrane concentration of liquid foods by forward osmosis: Process and quality view, *J. Food Eng.*, 2012, **111**, 483–489, DOI: 10.1016/J.JFOODENG.2012.01.032.
7 Q. She, Y. K. W. Wong, S. Zhao and C. Y. Tang, Organic fouling in pressure retarded osmosis: Experiments, mechanisms and implications, *J. Membr. Sci.*, 2013, **428**, 181–189, DOI: 10.1016/J.MEMSCI.2012.10.045.
8 X. Zhang, S. Xiong, C. X. Liu, L. Shen, C. Ding, C. Y. Guan and Y. Wang, Confining migration of amine monomer during interfacial polymerization for constructing thin-film composite forward osmosis membrane with low fouling propensity, *Chem. Eng. Sci.*, 2019, **207**, 54–68, DOI: 10.1016/J.CES.2019.06.010.
9 D. Li, Y. Yan and H. Wang, Recent advances in polymer and polymer composite membranes for reverse and forward osmosis processes, *Prog. Polym. Sci.*, 2016, **61**, 104–155, DOI: 10.1016/J.PROGPOLYMSCI.2016.03.003.

10 H. Jain, A. Kumar, V. D. Rajput, T. Minkina, A. K. Verma, S. Wadhwa, R. Dhupper, M. C. Garg and H. Joshi, Fabrication and characterization of high-performance forward-osmosis membrane by introducing manganese oxide incited graphene quantum dots, *J. Environ. Manage.*, 2022, **305**, 114335, DOI: 10.1016/J.JENVMAN.2021.114335.

11 P. Oymaci, K. Nijmeijer and Z. Borneman, Development of Polydopamine Forward Osmosis Membranes with Low Reverse Salt Flux, *Membranes*, 2020, **10**, 94, DOI: 10.3390/MEMBRANES10050094.

12 H. Salehi, M. Rastgar and A. Shakeri, Anti-fouling and high water permeable forward osmosis membrane fabricated via layer by layer assembly of chitosan/graphene oxide, *Appl. Surf. Sci.*, 2017, **413**, 99–108, DOI: 10.1016/J.APSUSC.2017.03.271.

13 M. Li, V. Karanikola, X. Zhang, L. Wang and M. Elimelech, A Self-Standing, Support-Free Membrane for Forward Osmosis with No Internal Concentration Polarization, *Environ. Sci. Technol. Lett.*, 2018, **5**, 266–271, DOI: 10.1021/ACS.ESTLETT.8B00117.

14 L. Shen, W. S. Hung, J. Zuo, L. Tian, M. Yi, C. Ding and Y. Wang, Effect of ultrasonication parameters on forward osmosis performance of thin film composite polyamide membranes prepared with ultrasound-assisted interfacial polymerization, *J. Membr. Sci.*, 2020, **599**, 117834, DOI: 10.1016/J.MEMSCI.2020.117834.

15 G. Han, S. Zhang, X. Li, N. Widjojo and T. S. Chung, Thin film composite forward osmosis membranes based on polydopamine modified polysulfone substrates with enhancements in both water flux and salt rejection, *Chem. Eng. Sci.*, 2012, **80**, 219–231, DOI: 10.1016/J.CES.2012.05.033.

16 D. L. Shaffer, J. R. Werber, H. Jaramillo, S. Lin and M. Elimelech, Forward osmosis: Where are we now?, *Desalination*, 2015, **356**, 271–284, DOI: 10.1016/j.desal.2014.10.031.

17 J. Zhou, H. L. He, F. Sun, Y. Su, H. Y. Yu and J. S. Gu, Structural parameters reduction in polyamide forward osmosis membranes via click modification of the polysulfone support, *Colloids Surf., A*, 2020, **585**, 124082, DOI: 10.1016/j.colsurfa.2019.124082.

18 P. Lu, W. Li, S. Yang, Y. Wei, Z. Zhang and Y. Li, Layered double hydroxides (LDHs) as novel macropore-templates: The importance of porous structures for forward osmosis desalination, *J. Membr. Sci.*, 2019, **585**, 175–183, DOI: 10.1016/j.memsci.2019.05.045.

19 K. Zheng, S. Zhou and X. Zhou, High-performance thin-film composite forward osmosis membrane fabricated on low-cost PVB/PVC substrate, *RSC Adv.*, 2018, **42**(16), 13382–13392, DOI: 10.1039/C8NJ01677A.

20 P. R. Gulave and S. Y. Guhe, An overview of recent advances in inorganic nanomaterials and MOFs in modification of Forward osmosis membranes for Industrial Wastewater Treatment, *J. Inorg. Organomet. Polym. Mater.*, 2025, **35**, 1453–1474, DOI: 10.1007/s10904-024-03353-4.

21 P. Lu, S. Liang, T. Zhou, T. Xue, X. Mei and Q. Wang, Layered double hydroxide nanoparticle modified forward osmosis membranes via polydopamine immobilization with significantly enhanced chlorine and fouling resistance, *Desalination*, 2017, **421**, 99––109, DOI: 10.1016/j.desal.2017.04.030.

22 M. Rastgar, A. Shakeri, A. Bozorg, H. Salehi and V. Saadattalab, Impact of nanoparticles surface characteristics on pore structure and performance of forward osmosis membranes, *Desalination*, 2017, **421**, 179–189, DOI: 10.1016/j.desal.2017.01.040.

23 M. J. Park, S. Phuntsho, T. He, G. M. Nisola, L. D. Tijing, X. M. Li, G. Chen, W. J. Chung and H. K. Shon, Graphene oxide incorporated polysulfone substrate for the fabrication of flat-sheet thin-film composite forward osmosis membranes, *J.Membr.Sci*, 2015, **493**, 496–507, DOI: 10.1016/j.memsci.2015.06.053.

24 M. N. Li, X. J. Chen, Z. H. Wan and S. G. Wang, Forward osmosis membranes for high-efficiency desalination with Nano-MoS2 composite substrates, *Chemosphere*, 2021, **278**, 130341, DOI: 10.1016/j.chemosphere.2021.130341.

25 H. Salehi, A. Shakeri and S. R. Razavi, Polyethersulfone–Quaternary Graphene Oxide–Sulfonated Polyethersulfone as a High-Performance Forward Osmosis Membrane Support Layer, *ACS ES&T Water*, 2022, **2**(4), 508–517, DOI: 10.1021/acsestwater.1c00249.

26 Y. Wang, R. Ou, Q. Ge, H. Wang and T. Xu, Preparation of polyethersulfone/carbon nanotube substrate for high-performance forward osmosis membrane., *Desalination*, 2013, **330**, 70–78, DOI: 10.1016/j.desal.2013.09.028.

27 D. Ma, G. Han, S. B. Peh and S. B. Chen, Water-stable metal–organic framework UiO-66 for performance enhancement of forward osmosis membranes, *Ind. Eng. Chem. Res.*, 2017, **56**(44), 12773–12782, DOI: 10.1021/acs.iecr.7b03278.

28 R. Ramezani Darabi, M. Peyravi and M. Jahanshahi, Modified forward osmosis membranes by two amino-functionalized ZnO nanoparticles: A comparative study, *Chem. Eng. Res. Des.*, 2019, **145**, 85–98, DOI: 10.1016/j.cherd.2019.02.019.

29 Y. Li, G. He, S. Wang, S. Yu, F. Pan, H. Wu and Z. Jiang, Recent advances in the fabrication of advanced composite membranes, *J. Mater. Chem. A*, 2013, **1**, 10058–10077, DOI: 10.1039/C3TA01652H.

30 S. F. Chua, K. M. Lam, A. Nouri, E. Mahmoudi, W. L. Ang, W. J. Lau and A. W. Mohammad, Effect of poly(2-(dimethylamino)ethyl methacrylate) brush-grafted graphene oxide on polyamide layer formation and nanofiltration performance, *J. Environ. Chem. Eng.*, 2024, **12**, 111935, DOI: 10.1016/J.JECE.2024.111935.

31 S. R. Razavi, A. Shakeri and H. Mahdavi, Polymer-grafted graphene oxide as a high-performance nanofiller for modification of forward osmosis membrane substrates, *ACS. Appl.Polym.Mater*, 2022, **4**(12), 8878–8891, DOI: 10.1021/acsapm.2c01266.

32 R. Razavi, H. Salehi and A. Shakeri, A novel thin film nanocomposite forward osmosis membrane modified with zwitterionic GO-g-PSBMA with high fouling resistance and heavy metal ions rejection, *J. Environ. Chem. Eng.*, 2025, **13**(1), 115308, DOI: 10.1016/j.jece.2025.115308.
33 C. H. Du, X. Y. Zhang and C. J. Wu, Chitosan-modified graphene oxide as a modifier for improving the structure and performance of forward osmosis membranes, *Polym. Adv. Technol.*, 2020, **31**(4), 807–816, DOI: 10.1002/pat.4816.
34 T. Ghanbari, A. Sharif and M. Karimi, Polysulfone substrates modified with polyethylene glycol-grafted graphene oxide nanosheets for enhanced forward osmosis performance, *ChERD*, 2025, **217**, 223–234, DOI: 10.1016/j.cherd.2025.03.032.
35 D. C. Marcano, D. V. Kosynkin, J. M. Berlin, A. Sinitskii, Z. Sun, A. Slesarev, L. B. Alemany, W. Lu and J. M. Tour, Improved synthesis of graphene oxide, *ACS nano*, 2020, **4**(8), 4806–4814, DOI: 10.1021/nn1006368.
36 S. Mushtaq, N. M. Ahmad, A. Mahmood and M. Iqbal, Antibacterial amphiphilic copolymers of dimethylamino ethyl methacrylate and methyl methacrylate to control biofilm adhesion for antifouling applications, *Polymers*, 2021, **13**(2), 216, DOI: 10.3390/polym13020216.
37 M. Muniyalakshmi, K. Sethuraman and D. Silambarasan, Synthesis and characterization of graphene oxide nanosheets, *Mater. Today*, 2020, **21**, 408–410, DOI: 10.1016/j.matpr.2019.06.375.
38 J. Mao, X. Ji and S. Bo, Synthesis and pH/Temperature-Responsive Behavior of PLLA-b-PDMAEMA Block Polyelectrolytes Prepared via ROP and ATRP, *Macromol. Chem. Phys.*, 2011, **212**(7), 744–752, DOI: 10.1002/macp.201000672.
39 P. N. Diagboya, H. K. Mmako, E. D. Dikio and F. M. Mtunzi, Synthesis of amine and thiol dual functionalized graphene oxide for aqueous sequestration of lead, *J. Environ. Chem. Eng.*, 2019, **7**, 103461, DOI: 10.1016/J.JECE.2019.103461.
40 R. Feng, W. Zhou, G. Guan, C. Li, D. Zhang, Y. Xiao, L. Zheng and W. Zhu, Surface decoration of graphene by grafting polymerization using graphene oxide as the initiator, *J. Mater. Chem.*, 2012, **22**, 3982–3989, DOI: 10.1039/C2JM13667H.
41 M. Namvari, C. S. Biswas, M. Galluzzi, Q. Wang, B. Du and F. J. Stadler, Reduced graphene oxide composites with water soluble copolymers having tailored lower critical solution temperatures and unique tube-like structure, *Sci. Rep.*, 2017, **7**, 1–9, DOI: 10.1038/srep44508.
42 A. Das, N. Mukherjee and T. Jana, Polymer-Grafted Graphene Oxide/Polybenzimidazole Nanocomposites for Efficient Proton-Conducting Membranes, *ACS Appl. Nano Mater.*, 2023, **6**, 6365–6379, DOI: 10.1021/ACSANM.3C00834.
43 H. Wang, X. Lu, X. Lu, Z. Wang, J. Ma and P. Wang, Improved surface hydrophilicity and antifouling property of polysulfone ultrafiltration membrane with poly(ethylene glycol) methyl ether methacrylate grafted graphene oxide nanofillers, *Appl. Surf. Sci.*, 2017, **425**, 603–613, DOI: 10.1016/J.APSUSC.2017.06.292.
44 H. Wu, J. Mansouri and V. Chen, Silica nanoparticles as carriers of antifouling ligands for PVDF ultrafiltration membranes, *J. Membr. Sci.*, 433, **433**, 135–151, DOI: 10.1016/j.memsci.2013.01.029.
45 D. Emadzadeh, W. J. Lau, T. Matsuura, M. Rahbari-Sisakht and A. F. Ismail, A novel thin film composite forward osmosis membrane prepared from PSf–TiO_2 nanocomposite substrate for water desalination, *Chem. Eng. J.*, 2014, **237**, 70–80, DOI: 10.1016/J.CEJ.2013.09.081.
46 V. Vatanpour, S. S. Madaeni, R. Moradian, S. Zinadini and B. Astinchap, Fabrication and characterization of novel antifouling nanofiltration membrane prepared from oxidized multiwalled carbon nanotube/polyethersulfone nanocomposite, *J. Membr. Sci.*, 2011, **375**, 284–294, DOI: 10.1016/J.MEMSCI.2011.03.055.
47 M. Kumar, Z. Gholamvand, A. Morrissey, K. Nolan, M. Ulbricht and J. Lawler, Preparation and characterization of low fouling novel hybrid ultrafiltration membranes based on the blends of GO–TiO_2 nanocomposite and polysulfone for humic acid removal, *J. Membr. Sci.*, 2016, **506**, 38–49, DOI: 10.1016/J.MEMSCI.2016.02.005.
48 M. Corvilain, C. Klaysom, A. Szymczyk and I. F. J. Vankelecom, Formation mechanism of sPEEK hydrophilized PES supports for forward osmosis, *Desalination*, 2017, **419**, 29–38, https://doi.org/10.1016/J.DESAL.2017.05.037.
49 X. Huang, B. T. McVerry, C. Marambio-Jones, M. C. Y. Wong, E. M. V. Hoek and R. B. Kaner, Novel chlorine resistant low-fouling ultrafiltration membrane based on a hydrophilic polyaniline derivative, *J. Mater. Chem. A*, 2015, **3**, 8725–8733, DOI: 10.1039/C5TA00900F.
50 X. Wen, C. He, Y. Hai, R. Ma, J. Sun, X. Yang, Y. Qi, H. Wei and J. Chen, Fabrication of an antifouling PES ultrafiltration membrane via blending SPSF, *RSC Adv.*, 2022, **12**(3), 1460–1470, DOI: 10.1039/D1RA06354E.
51 P. Wang, J. Ma, Z. Wang, F. Shi and Q. Liu, Enhanced separation performance of PVDF/PVP-g-MMT nanocomposite ultrafiltration membrane based on the NVP-grafted polymerization modification of montmorillonite (MMT), *Langmuir*, 2012, **28**, 4776–4786, DOI: 10.1021/LA203494Z/SUPPL_FILE/LA203494Z_SI_001.PDF.
52 X. Zhang, L. Shen, C. Y. Guan, C. X. Liu, W. Z. Lang and Y. Wang, Construction of SiO_2@MWNTs incorporated PVDF substrate for reducing internal concentration polarization in forward osmosis, *J. Membr. Sci.*, 2018, **564**, 328–341, DOI: 10.1016/j.memsci.2018.07.043.
53 C. Klaysom, S. Hermans, A. Gahlaut, S. Van Craenenbroeck and I. F. J. Vankelecom, Polyamide/Polyacrylonitrile (PA/PAN) thin film composite osmosis membranes: Film optimization, characterization and performance evaluation, *J. Membr. Sci.*, 2013, **445**, 25–33, DOI: 10.1016/J.MEMSCI.2013.05.037.
54 M. Fathizadeh, A. Aroujalian and A. Raisi, Effect of lag time in interfacial polymerization on polyamide composite membrane

with different hydrophilic sub layers, *Desalination*, 2012, **284**, 32–41, DOI: 10.1016/J.DESAL.2011.08.034.

55 K. Zheng, S. Zhou, Z. Cheng and G. Huang, Polyvinyl chloride/quaternized poly phenylene oxide substrates supported thin-film composite membranes: Enhancement of forward osmosis performance, *J. Membr. Sci.*, 2021, **623**, 119070, DOI: 10.1016/J.MEMSCI.2021.119070.

56 S. Zhao, N. Sun, P. Dou, S. Lin and T. He, Structure parameter as an intrinsic property of thin-film composite forward osmosis membrane, *Desalination*, 2024, **581**, 117616, DOI: 10.1016/j.desal.2024.117616.

57 L. Huang, J. T. Arena and J. R. McCutcheon, Surface modified PVDF nanofiber supported thin film composite membranes for forward osmosis, *J. Membr. Sci.*, 2016, **499**, 352–360, DOI: 10.1016/J.MEMSCI.2015.10.030.

58 J. Li, Q. Liu, X. Li, Y. Liu and J. Xie, Template-Assisted Fabrication of Thin-Film Composite Forward-Osmosis Membrane with Controllable Internal Concentration Polarization, *Ind. Eng. Chem. Res.*, 2016, **55**, 5327–5334, DOI: 10.1021/ACS.IECR.6B00874/SUPPL_FILE/IE6B00874_SI_001.PDF.

59 A. Arjmandi, M. Peyravi and A. Altaee, Exploring the use of cheap natural raw materials to reduce the internal concentration polarization in thin-film composite forward osmosis membranes, *Chem. Eng. J.*, 2020, **398**, 125483, DOI: 10.1016/j.cej.2020.125483.

60 A. Hosseinzadeh, A. Altaee, I. Ibrar and J. L. Zhou, Modeling and optimization of reverse salt diffusion and water flux in forward osmosis by response surface methodology and artificial neural network, *Chemical Engineering and Processing-Process Intensification*, 2025, **208**, 110140, DOI: 10.1016/j.cep.2024.110140.

61 Y. Wang, R. Ou, H. Wang and T. Xu, Graphene oxide modified graphitic carbon nitride as a modifier for thin film composite forward osmosis membrane, *J. Membr. Sci.*, 2015, **475**, 281–289, DOI: 10.1016/J.MEMSCI.2014.10.028.

62 P. Lu, S. Liang, T. Zhou, X. Mei, Y. Zhang, C. Zhang, A. Umar and Q. Wang, Layered double hydroxide/graphene oxide hybrid incorporated polysulfone substrate for thin-film nanocomposite forward osmosis membranes, *RSC Adv.*, 2016, **6**, 56599–56609, DOI: 10.1039/C6RA10080E.